Visualizing reaction and diffusion in xanthan gum aerosol particles exposed to ozone

Visualizing Reaction and Diffusion in Xanthan Gum Aerosol Particles Exposed to Ozone

Peter A. Alpert*[a], Pablo Corral Arroyo[a,b], Jing Dou[c], Ulrich K. Krieger[c], Sarah S. Steimer[d], Jan-David Förster[e], Florian Ditas[e], Christopher Pöhlker[e], Stéphanie Rossignol[f,g], Monica Passananti[f,h,i], Sebastien Perrier[f], Christian George[f], Manabu Shiraiwa[j], Thomas Berkemeier[k], Benjamin Watts[l] and Markus Ammann*[a]

[a]Laboratory of Environmental Chemistry, Paul Scherrer Institute, 5232 Villigen PSI, Switzerland

[b]Institute for Atmospheric and Climate Science, ETH Zürich, 8092 Zürich, Switzerland.

[c]Institute for Physical Chemistry, ETH Zürich, 8092 Zürich, Switzerland.

[d]Department of Chemistry, University of Cambridge, Cambridge, CB2 1EW, United Kingdom.

[e]Multiphase Chemistry Department, Max Planck Institute for Chemistry, 55128 Mainz, Germany.

[f]Univ. Lyon, Université Claude Bernard Lyon 1, CNRS, IRCELYON, F-69626, Villeurbanne, France

[g]Aix Marseille Université, CNRS, LCE UMR 7376, 13331 Marseille, France.

[h]Institute for Atmospheric and Earth System Research/Physics, Faculty of Science, University of Helsinki, 00710, Helsinki, Finland

[i]Dipartimento di Chimica, Università di Torino, Via Giuria 5, 10125 Torino, Italy

[j]Department of Chemistry, University of California, Irvine, CA 92617, United States

[k]School of Chemical & Biomolecular Engineering, Georgia Institute of Technology, Atlanta, GA 30332, United States

[l]Laboratory for Synchrotron Radiation-Condensed Matter, Paul Scherrer Institute, 5232 Villigen PSI, Switzerland

† Electronic Supplementary Information (ESI) available. See DOI: 10.1039/cXCP00000x/

*Corresponding authors Peter.Alpert@psi.ch and Markus.Ammann@psi.ch

1 Abstract

Atmospheric aerosol particles are composed of inorganic and organic compounds. The latter can have a high viscosity that can lead to low molecular diffusion in particles and slower chemical reactions than what would be expected if particles were assumed to be in equilibrium with the gas phase following Henry's Law and reactants were considered to be well-mixed. Heterogeneous chemical reaction rates between gas phase oxidants and condensed phase reactants can be slowed when relative humidity decreases likely due to the loss of water and of its plasticizing effect on viscous organic matter. Models have predicted spatial concentration gradients in reactant concentration within particles depending on size as a consequence of this phenomena. However, these have never been observed for atmospherically relevant particle diameters. We investigated the reaction between ozone and aerosol particles composed of xanthan gum and $FeCl_2$ and observed the *in situ* chemical reaction that oxidized Fe^{2+} to Fe^{3+} using state of the art X-ray spectromicroscopy. Iron oxidation state of particles as small as 0.2 μm in diameter were chemically mapped for hours with time resolution on the scale of minutes and spatial scales of tens of nanometers. We found the loss of Fe^{2+} accelerated not only when ozone concentration increased from 100 to 2000 ppb, but also when relative humidity, RH, increased from 0 to 80% at 20° C. We calculated the Fe^{2+} fraction, α, out of the total iron and developed a unique analytical procedure to derive concentric 2-D column integrated profiles with high accuracy. We demonstrated that particle surfaces became oxidized while the core remained completely unreacted at $RH = 0 - 20\%$. At $RH = 40 - 80\%$, gradients in α developed over time, e.g. where $\alpha = 0.1$ and 0.5 at the surface and center, respectively, of a 1 μm diameter particle. We used the kinetic multi-layer model for aerosol surface and bulk chemistry (KM-SUB) to simulate reaction constrained with our observations and inferred key parameters as a function of RH including Henry's Law constant for ozone, H_{O_3}, and diffusion coefficients for ozone and iron, D_{O_3} and D_{Fe}, respectively. In order to reproduce our observed gradients, it was determined that ozone could not be present further than a few nanometers from a particle surface. This result led us to suspect that our system could be described with a reacto-diffusive framework, which is an analytical solution to the time rate of change of α, requires no computational effort compared to KM-SUB and relies on measurable physical parameters. We compared our data with theoretical and model prediction and found that within our experimental uncertainty, the reacto-diffusive framework is valid for our reactive

system. A discussion of other reactive systems of atmospheric importance and why a reacto-diffusive framework may be pervasive in aerosol chemistry is presented. Our results have vast implications e.g. for predicting aerosol toxicity changes, loss rate of known tracer compounds to track air mass origin and other aerosol compositional changes important for light scattering and cloud formation.

2 Introduction

Organic matter in atmospheric aerosol stems from a variety of natural and anthropogenic sources and is found in significant quantities in almost every single particle[1–3]. Aerosol particles can both scatter and absorb light to varying degrees depending on their morphology and chemical composition, and they significantly impact the global radiative balance[4,5]. These particles also act as nuclei for liquid droplets and ice in clouds[6–8]. The fate of aerosol particles residing in the atmosphere is largely dependent on physical processes such as rain out and gravitational settling, but also on chemical transformation[9]. The composition of particles, largely organic and inorganic species such as sulfate, nitrate, ammonium, sea salts and trace metals, is linked with uptake and internal production of oxidants leading to significant chemical change[10]. In sea spray aerosol, for example, chemical reactions can increase hydrophilicity and hence more efficient cloud condensation nuclei[11]. On the other hand, less hygroscopic particles can result from first condensing organic acids, then chlorine displacement and finally the formation of sodium-organic salts that take up less water than marine halides[11,12]. Organic matter in atmospheric aerosol particles can be highly viscous with physical properties similar to glass or tar, or they can exist in a more liquid-like state depending on location, altitude, temperature and relative humidity[13,14]. Molecules reacting in highly viscous particles can be diffusion limited, for example when the motion of two species and the rate at which they meet is much slower than the rate at which they react with each other. This results in a reduced overall rate of reaction[14,15]. There is a wealth of research into the effects of this phenomenon on chemical and physical aerosol processes and includes, in part, aerosol growth after nucleation[16–18], water uptake and ice nucleation[7], preservation and transport of biomass burning tracer compounds[19] or pollutants[20,21] and nutrient input into marine ecosystems[22].

Oxidants such as OH[23–33] and O_3[34–39] reacting with micrometer and submicrometer sized organic aerosol particles in a humidified environment have been previously observed and modeled to increase

our understanding of how these small molecules may diffuse through and react within atmospheric particles. Further studies have made great strides in developing model frameworks to describe experimental data, including modeling of chemical reactions at the surface and within the bulk of aerosol particles[27,30,33,34,40–50]. In the study of Shiraiwa *et al.*[34], the chemical half life of amino acids in thin films of bovine serum albumin (BSA) at a relative humidity, RH, of 90% and temperature, T, of 25 °C was determined to be about 5 min and increased to over an hour when $RH < 50\%$. These authors used the kinetic multi-layer model for aerosol surface and bulk chemistry (KM-SUB) to attribute this RH dependence on inhomogeneous mixing of reactants and products and calculated that at $RH = 50\%$, the BSA diffusion coefficient was 10^{-20} cm^2 s^{-1} with a viscosity close to that of a glass[34]. Ozone had a diffusion coefficient of 10^{-9} cm^2 s^{-1} and was predicted only to be present and reacting in the first tens of nanometers of the BSA films[34]. Heine *et al.*[39] found that the decay of squalene reacting with O_3 over time was identical over the RH range of $0 - 60\%$ leading them to use a stochastic multilayer model, Kinetiscope, to reproduce their results having a 1 nm adsorption layer coupled to a bulk reaction scheme. Reaction of O_3 was predicted to mainly occur in this adsorption layer[39]. This was supported by the authors' previous studies[38] and calculations of O_3 diffusion during reaction observed for particles with a $1 - 2$ nm squalene coating[51]. In an earlier study by Steimer *et al.*[36], shikimic acid particles were chemically imaged with scanning transmission X-ray microscopy coupled to near-edge X-ray absorption fine structure spectroscopy (STXM/NEXAFS) during O_3 exposure as a function of RH. The authors directly probed the C=C $1s \rightarrow \pi^*$ electronic transition and observed that reactive decay was highly dependent on RH, where shikimic acid lifetime increased 3 orders of magnitude when RH was lowered from 82 to 12%. Later, Steimer *et al.*[37] measured O_3 reactive uptake coefficients to shikimic acid in a comprehensive data set with high time resolution over seconds to 14 hr at $RH = 92$, 83, 68, 45, 24 and 0%, a constant O_3 gas phase concentration, $[O_3]_g = 178$ ppb and additionally for various $[O_3]_g = 79$, 178, 495 and 1985 ppb at $RH = 92$ and 24%. This data set was a benchmark for a later modeling study by Berkemeier *et al.*[47] using KM-SUB, who were able to determine physico-chemical parameters with high confidence such as chemical reaction kinetics of shikimic acid and reactive oxygen intermediates as well as changes in particle phase and molecular transport of O_3, all of which would have otherwise been impossible under a narrow experimental range of RH, time and $[O_3]_g$.

Observations and models mentioned above gave great insight to how molecules react and diffuse in

aerosol particles, however direct observation of particle internal concentration gradients of reactants or products to compare against any model predictions was lacking until now. We present a study in which O_3 diffusion and reaction in organic aerosol particles was tracked over time and imaged *in situ* (while O_3 exposure was taking place) at different RH and $[O_3]_g$. This was accomplished using STXM/NEXAFS to produce chemical images of particles at a pixel size of 35 nm, meaning that locations where O_3, reactant and product molecules diffused and reacted could be directly observed inside of particles. Steimer *et al.*[36] were the first to attempt such a measurement. In a scenario where O_3 reaction is fast compared to its diffusion, referred to as a reacto-diffusive limitation, O_3 should not penetrate far into the particle interior. Instead, O_3 would be limited to a characteristic length scale known as the reacto-diffusive length, which depends on its diffusion coefficient and first order loss rate[36]. More precisely, it is the distance over which O_3 concentration in the condensed phase, $[O_3]$, drops by a factor of $1/e$. In Steimer *et al.*[36], imaged chemical gradients in C=C absorption signal were not discernible. Considering their uncertainties due to image alignment, a low X-ray signal at thin particle edges and a limit on the contrast between C=C absorption and total carbon, these authors hypothesized that shikimic acid diffusion may have been fast enough to result in uniform profiles[36].

In this study, we exposed particles composed of a mixture of xanthan gum (XG) and $FeCl_2$ to O_3 and observed internal chemical reaction gradients over time, t. Iron in $FeCl_2$ has an oxidation state of +2 and transitions to an oxidation state of +3 when reacted with O_3, i.e. from Fe^{2+} to Fe^{3+} [52–56]. The use of iron in particles is a major benefit when employing STXM/NEXAFS due to the fact that X-ray absorption peaks are strong, narrow and thus can be observed with much higher contrast to detect Fe^{2+} and Fe^{3+} compared to the absorption from carbon functionalities such as C=C used in previous measurements[36,38]. Additionally, we built on previous work[57] and developed novel experimental and analytical procedures to quickly and efficiently quantify Fe^{2+} and Fe^{3+} for thousands of individual particles with a well-constrained uncertainty. In general, Fe containing aerosol particles are important e.g. for their role in ocean fertilization and stimulating the growth of phytoplankton[58]. Iron oxidation state can affect iron solubility, and iron can bind with organic ligands in atmospheric or oceanic particles influencing bioavailability in aquatic ecosystems[22,59–65]. Moffet *et al.*[57] used STXM/NEXAFS to quantify the Fe^{2+} fraction, α, out of the total iron in ambient particles and calculated an average mass weighted value of $\alpha = 0.33 \pm 0.08$ during a pollution transport event from China to Japan, of which $\sim 5\%$ of

particles contained detectable iron. We note that iron oxidation state from particle to particle varied and appeared inhomogeneously distributed in this ambient aerosol population[57]. As a polysaccharide and biopolymer, XG is a unique model compound of marine derived organic matter in atmospheric aerosol[66]. The change in XG composition by a few percent in water is enough to result in large changes in solution viscosity, a property that is highly desired for additives used in the food industry[67,68]. XG hygroscopicity is of particular interest as decreasing RH leads to decreasing water content and increasing viscosity[66,69]. We note that XG is a reference compound for quantifying what is known as "transparent exopolymer particles" in oceans[70–72] which has recently been found in ambient air at concentrations of 2 μg m^{-3} in the North Atlantic ocean[73]. For these reasons, the XG/Fe^{2+} system is an interesting proxy for understanding molecular diffusion and reaction in atmospheric marine derived aerosol.

Here, we used iron as a tracer for STXM/NEXAFS to unambiguously identify the spatial location within particles where oxidation reactions took place. These data were used to experimentally derive 2-D projected α profiles within thousands of individual particles *in situ* yielding the first direct evidence of chemical reaction gradients in viscous particles. We report on how gradients change when particles were dry ($RH = 0\%$) or humidified at $RH = 20$, 40, 60 and 80%. KM-SUB was used to model diffusion and reaction in spherical shells of aerosol particles and derived 3-D radial profiles of α using known chemical reaction rates. These 3-D α profiles were then used to calculate 2-D column integrated profiles of α for direct comparison with STXM/NEXAFS observations. Model parameters were diffusion coefficients for Fe and O_3, D_{Fe} and D_{O_3}, respectively, and were described with a Vignes-type equation as a function of water mole fraction. Henry's Law constant for O_3 in the XG/$FeCl_2$ matrix, H_{O_3}, was also derived. We claim our STXM/NEXAFS spatio-chemical data allows a unique and exact constraint for modeling aerosol internal chemical profiles, i.e. simultaneous reproduction of bulk Fe^{2+} depletion and the spatio-temporal evolution of O_3 and Fe^{2+} reaction. In the context of our results, we discuss the applicability of the reacto-diffusive limiting case and the importance of direct observational constraints on model predictions of atmospheric aerosol chemical aging.

3 Results and Discussion

3.1 NEXAFS spectra

Figure 1 shows example NEXAFS spectra of oxidized XG/$FeCl_2$ particles at dry and humidified conditions in comparison with the reference material $FeCl_2$ measured here and $FeCl_2$ and $FeCl_3$ from literature[57]. Two absorption peaks at 707.8 and 709.6 eV were observed for oxidized XG/$FeCl_2$ particles and were in agreement with Fe^{2+} and Fe^{3+} peak absorption energies for $FeCl_2$ and $FeCl_3$, respectively. The nearly identical peak positions may indicate that humidity and the organic polysaccharide matrix does not influence Fe electronic excitations. Important to note from Fig. 1 is that only Fe^{2+} and Fe^{3+} peaks were observed in oxidized particles meaning that the total Fe concentration, $[Fe_{tot}]=[Fe^{2+}]+[Fe^{3+}]$, where $[Fe^{2+}]$ and $[Fe^{3+}]$ is the concentration of Fe^{2+} and Fe^{3+} species, respectively, and

$$\alpha = [Fe^{2+}]/[Fe_{tot}]. \quad (1)$$

We note that X-ray absorption at the Fe L-edge was observed homogeneously and never in dense localized regions (i.e. as immersed iron nanoparticles) indicating that iron was well-mixed in our experiments.

3.2 Xanthan gum/$FeCl_2$ particles exposed to oxygen

Using the parameterization from Moffet *et al.*[57], α was determined from measuring the peak optical density, OD, corresponding to Fe^{2+} and Fe^{3+} indicated in Fig. 1 and taking their ratio, r. Details in calculating r and α are given in the ESI†, in addition to a careful assessment of X-ray exposure used as to not damage the particles while maximizing signal (see Figs. S1 and S2). We performed exposure experiments of XG/$FeCl_2$ particles to O_2 at various RH and calculated α as a function of t. Figure S3 shows that when exposed only to O_2, no change in α was observed at any RH investigated. Therefore, any reaction taking place between O_2 and Fe^{2+} in our particles over t was negligible. The scatter in α for O_2 exposure mostly fell within ± 0.07, which was the standard deviation of α for individual particles with a diameter, d_p, seen in Fig. S4 in the ESI†. It is apparent that α values for larger particles have a smaller error. This is due to both the greater number of pixels and the greater signal statistics provided by the greater thickness of these particles. Particles with $d_p < 0.2$ μm (not shown) were discarded

from our analysis because their error was typically larger than any physically realistic range in α. The standard deviation of each data set indicated in Fig. S4 and plotted in Fig. S3 was typically larger than the error propagated through quadrature. For the remainder of the manuscript, error bars on all α values are either ± 0.07 or the propagated error, whichever is greater.

3.3 Oxidation of xanthan gum/$FeCl_2$ particles by ozone.

Figure 2 shows α averaged over all particles as a function of time, ozone exposure, χ, and RH. The most striking result is that under dry conditions where $RH = 0$ and 20%, very little change in α was observed. At more humid conditions of $RH = 40$, 60 and 80%, average α values decreased noticeably over t. Although the green circles for $RH = 60\%$ shows the greatest decrease in α, this is a consequence of using higher $[O_3]_g$ (see Fig. S5 in the ESI†). At $RH = 0$, 20 and 60%, shown as red, pink and green circles, respectively, $[O_3]_g$ was on the order of 10^3 ppb which was about 10 times higher than for $RH = 40$ and 80%. Figure 2b shows α as a function of $\chi = \int [O_3]_g(t) \cdot dt$, where $[O_3]_g(t)$ is taken from Fig. S5. Iron oxidation was greater at $RH = 80\%$ than any other RH as a function of χ. This can be seen in particular at $\chi = 10^{-3}$ atm s, where the blue symbols reach $\alpha = 0.3$ while all other data at $RH < 80\%$ have higher α. In general, as RH or $[O_3]_g$ increased, O_3 heterogeneous reaction rates must have also increased.

We acquired high spatial resolution chemical images to quantify α over the particles in two dimensions. To accomplish this, α was averaged over all pixels identified at the perimeter of particles irrespective of particle size. In other words, α was calculated from the particle perimeter to 1 pixel, or 35 nm, from the surface. Then, all adjacent concentric pixels toward the particle center (from 1 to 2 pixels from the particle surface or 35-70 nm) were identified and their corresponding α values averaged. This continued toward the center of particles and generated a 2-D concentric profile of α, which is also a column integrated profile.

Figure 3 shows 2-D profiles of α as a function of time and the pixels (distance) from the perimeter of particles for all experiments. More oxidation occurred at the perimeter than at the center of particles, and the reaction gradients were typically shallow for all RH. For example, α increased from 0.45 to 0.65 at $RH = 40\%$ and $t = 180$ min (orange symbol color in Fig. 3c) over ~ 0.5 μm. At $RH = 80\%$, α

increased from 0.25 to 0.35 for the same reaction time and distance. For $RH = 0$ and 20%, α increased by about over a length scale of ~ 0.2 μm, implying a stronger Fe^{2+} concentration gradient under dry conditions than for more humid conditions. Prior to exposure, initial values of α were not equivalent to 1, implying that the short time ($\sim$ 30 minutes) spent in contact in ambient laboratory air was enough to trigger particle oxidation. We caution studies determining Fe oxidation state changes during exposure experiments in a laboratory setting. We quantified initial α prior to O_2 and O_3 exposure to ensure a high enough value for experiments.

Observed 2-D profiles were likely to be influenced by 4 factors. The first is the plasticizing effect water has on viscous XG-containing particles to the extent that a greater water content likely enhanced O_3 molecular diffusion. At low RH, D_{O_3} may have been low enough to limit penetration to the particle bulk for further reaction with Fe^{2+} in line with our observations that α was always less at particle surfaces than at their center. The glass transition temperature of XG (defined at a viscosity $> 10^{12}$ Pa s) was previously determined to be -16.4 and -23.3° C for RH of 84 and 11%, respectively[69]. Although our experiments were performed at 20° C which is significantly warmer than the glass transition temperature, we still expect sufficiently low diffusion to limit reactions due to the fact that XG is thermally stable and its viscosity does not change much with temperature[68,74]. Dawson *et al.*[66] extrapolated viscosity measurements in dilute XG aqueous solutions from Wyatt and Liberatore[75] to higher concentrations and $RH = 80\%$ obtaining 10^{13} Pa s at 20 °C. This is inline with our suggestion that XG remains highly viscous and possibly close to or in a glass-like state. The second is that H_{O_3} may increase under dry conditions in XG compared to water where the condensed phase ozone concentration, $[O_3] = H_{O_3}[O_3]_g$. This was observed previously for pure shikimic acid, that H_{O_3} in organic material was about an order of magnitude higher than for O_3 in water[36,47]. We note that both XG and shikimic acid can be considered an organic liquid with high viscosity with glass-like properties. Higher values of H_{O_3} may increase condensed phase O_3 concentration near the surface, increase the first order reaction rate there and cause stronger concentration gradients at low RH. A third reason for RH-dependent oxidation kinetics may also be due to change in the diffusion of Fe. As XG is a hydrogel material and takes up water in subsaturated conditions, we hypothesize that the Fe diffusion coefficient, D_{Fe}, should increase with increasing RH. A high value of D_{Fe} should result in more uniform α gradients, which is in line with out observations. The fourth is dilution with water at higher RH which should reduce the first order loss

rate, however we expect this to have little effect because oxidation was observed to proceed much faster under more humid conditions. We argue that faster diffusion of Fe^{2+} out of the particle core and faster diffusion of O_3 into the particle from the surface brings them together more readily allowing reactions to proceed at a faster rate.

3.4 Prediction of molecular diffusion and solubility

We have employed the KM-SUB model[47] to infer values of H_{O_3}, D_{O_3} and D_{Fe} which reproduce observed 2-D profiles in α. Although KM-SUB has been previously constrained with data relating to the uptake of gas phase oxidants by particles, our data set is unique in that it is the first study to present spatially-resolved condensed-phase concentration profiles. We reiterate that KM-SUB has predicted aerosol radial profiles[44,47,76] but up until now, have had no direct observational evidence that they existed. For direct comparison with our observed profiles in Fig. 3, radial profiles from KM-SUB were converted to 2-D hemispherical projections of α. This was accomplished by first determining the volume of every modeled spherical shell projected onto a 2-D grid point with the same resolution as the images acquired from STXM/NEXAFS. A graphical illustration is given in Fig. S6 of the ESI†. Each shell over a grid box (pixel) contributes a fraction of the total volume extending from the plate to the top of the particle. Therefore, α for a single grid point is calculated as the volume weighted average of each shell piece within a grid point. We have fit modeled 2-D profiles to our observations for all RH each having 4 optimized parameters, H_{O_3}, D_{O_3} and D_{Fe}, as well as the initial Fe^{2+} fraction, α_0. We note that α_0 was constrained by our observations and uncertainty. A brief description of all parameters used in KM-SUB is described below and their values can be found in Table 1.

A rate coefficient for O_3 and $FeCl_2$ was derived from previous studies[52–56] following,

$$Fe^{2+} + O_3 \longrightarrow FeO^{2+} + O_2, \tag{R1}$$

and

$$FeO^{2+} + Fe^{2+} \xrightarrow{2H+} 2\,Fe^{3+} + H_2O. \tag{R2}$$

The rate coefficient, k, for reaction R1 has been reported[52–56] in a range $k_{R1} = (1.7 - 8.2) \times 10^5$ M^{-1} s^{-1}.

Logager et al.[54] claimed reaction R2 should be the dominate sink for ferryl FeO^{2+} with $k_{R2} = 1.4 \times 10^5$ M^{-1} s^{-1} and excess of Fe^{2+}. The intermediate FeO^{2+} has been observed to act as an oxygen donor e.g. with dimethyl sulfoxide[55], however, no chemical kinetics have been measured with XG to our knowledge. Enami *et al.*[56] observed that FeO^{2+} was the main reactive intermediate produced during O_3 or H_2O_2 oxidation of $FeCl_2$ in solution. Earlier, Steigenberger *et al.*[77] observed no change in Fe^{2+} oxidation rates with H_2O_2 when XG was added. Due to the similarity of H_2O_2 and O_3 reaction with $FeCl_2$ to form ferryl iron, and due to the lack of reaction of the ferryl iron with XG when H_2O_2 was used, we expect that XG is not reactive with FeO^{2+} when O_3 was used in our experiments. We suspect XG is a poor oxygen acceptor and thus plays no role in oxidation with O_3. We note that $OH^{\cdot}$ was never observed as a product of O_3 reactions with $FeCl_2$, and Cl^- was previously found not to participate in the oxidation process[56]. Similarly, OH was not observed for O_2 reaction in aqueous $(NH_4)_2Fe(SO_4)_2$ solutions[54]. Aerosol particles used in our experiments had $[Fe^{2+}]$ on the order of 1 M implying that reaction R2 is very fast. Therefore, we suggest the net reaction

$$2\,Fe^{2+} + O_3 \xrightarrow{2H+} 2\,Fe^{3+} + O_2 + H_2O, \tag{R3}$$

where $k_{R3} = k_{\mathrm{R1}}$. We use $k_{R3} = 3.7 \times 10^5$ M^{-1} s^{-1} (which is the geometric mean of reported k_{R1} values) equivalent to 6.2×10^{-16} cm^3 s^{-1} indicated in Table 1 to model bulk O_3 reaction in our particles. The surface reaction rate coefficient is determined as $k_{\mathrm{slr1}} = \exp\left(\delta_{\mathrm{sh}} \ln k_{R3}\right) = 6.3 \times 10^{-14}$ cm^2 s^{-1}, where $\delta_{\mathrm{sh}} = 0.87$ is the ratio between the surface and bulk reaction rate of shikimic acid with O_3on a natural log scale. Parameters for O_3 utilized in KM-SUB are taken from previous work[47] and include the surface self reaction rate constant, k_{slr2}, the surface accommodation coefficient, $\alpha_{\mathrm{s,0}}$, the desorption lifetime, $\tau_{\mathrm{d,O_3}}$, the adsorption cross section for O_3, $\sigma_{\mathrm{O_3}}$ and the gas phase diffusion, $D_{\mathrm{g,O3}}$, at 150 mbar. The adsorption cross section for Fe, $\sigma_{\mathrm{Fe}} = 2 \times 10^{-16}$ cm^2, was taken from previous literature[78]. Parameters that depend on RH include the bulk to surface transfer rate, $k_{\mathrm{bs,O_3}}$, the surface to bulk transfer rate, $k_{\mathrm{sb,Fe}}$, and the equilibrium surface to bulk concentration ratio, K_{bs}, were determined from the following parameterizations fitted to previous values[47], where

$$k_{\mathrm{bs,O_3}} = 0.6904 + 1.1675e^{35.6235\left(\frac{RH}{100} - 0.8369\right)}, \tag{2}$$

$$\ln k_{\mathrm{sb,XG}} = -9.2911 + 7.0439\frac{RH}{100} - 5.4626\left(\frac{RH}{100}\right)^2 - e^{30.7316\left(\frac{RH}{100}-0.8484\right)}, \quad (3)$$

and

$$\ln K_{\mathrm{bs}} = -19.8434 - 1.5613\frac{RH}{100} + 3.1616\left(\frac{RH}{100}\right)^2, \quad (4)$$

which are shown in Fig. S7 of the ESI†. Water uptake of XG as a function of RH has been previously quantified using a hygroscopicity factor, $\kappa = 0.08$[66]. We calculated the water concentration in particles assuming XG contributes primarily to the water uptake and insignificantly from $FeCl_2$.

Figure 3 shows that the optimization of 2-D α profiles as solid lines agree well with our measurements, which is remarkable considering the large differences in $[O_3]_g$ and the long exposure time on the order of hours. Model predictions show steeper and shallower concentration gradients at lower and higher RH, respectively, in agreement with our observations. Consistently, Fe is predicted to remain more reduced in particle cores than at particle surfaces. Although not explicitly fit, the modeled α averaged over the entire particle, shown as solid lines in Fig. 2, captures the observed decay and reveals the consistency between modeled and measured α. The fitting parameters, H_{O_3}, D_{O_3} and D_{Fe} are given in Table 1 and shown in Fig. 4. We note that there is an obvious and expected trend that as RH decreases both D_{O_3} and D_{Fe} values decrease and H_{O_3} increases. We use a Vignes type equation to derive an expression for the fitting parameters continuous in RH in the following form,

$$\log D_{O_3} = (x_w\alpha_{x_w})\log D^{\circ}_{O_3} + (1 - x_w\alpha_{x_w})\log D_{O_3}(RH = 0\%), \quad (5)$$

$$\log D_{Fe} = (x_w\alpha_{x_w})\log D^{\circ}_{Fe} + (1 - x_w\alpha_{x_w})\log D_{Fe}(RH = 0\%), \quad (6)$$

$$\log H_{O_3} = (x_w\alpha_{x_w})\log H^{\circ}_{O_3} + (1 - x_w\alpha_{x_w})\log H_{O_3}(RH = 0\%), \quad (7)$$

and

$$\ln \alpha_{x_w} = (1 - x_w)^2[C + 3D - 4D(1 - x_w)], \quad (8)$$

where x_w is the mole fraction of water and $D_{O_3}(RH = 0\%)$, $D_{Fe}(RH = 0\%)$, $H_{O_3}(RH = 0\%)$, C and D are fitting parameters given in Table 2. Other parameters given in Table 2 are diffusion of O_3 in water, $D^{\circ}_{O_3}$, Henry's law coefficient of O_3 in water, $H^{\circ}_{O_3}$, and diffusion of Fe in water, D°_{Fe}. In terms of O_3

diffusion, observed D_{O_3} at $RH = 0\%$ was equal to 2.48×10^{-16} cm^2 s^{-1} and increased about 8 orders of magnitude to 4.17×10^{-8} cm^2 s^{-1} at $RH = 80\%$. At this high humidity, diffusion remains about 3 orders of magnitude less than $D^{\circ}_{O_3} = 1.9 \times 10^{-5}$ cm^2 s^{-1} taken from previous work[47,79]. In pure (dry) shikimic acid, $D_{O_3} = 2.90 \times 10^{-12}$ cm^2 s^{-1}, which is 4 orders of magnitude faster than for dry XG/$FeCl_2$ particles. This means O_3 diffusion in XG is less than for shikimic acid. A XG monomer is over 5 times the molar mass of shikimic acid and polymerization and cross-linking in XG can lead to an even higher molecular weight up to 2.9×10^6 g mol^{-1} [80]. Although diffusion coefficients of a small molecule is typically lower or higher through organic matter with higher or lower molar mass, respectively, following the Stokes-Einstein relation[81,82], care should be taken when extrapolating values as this is not always the case[83,84].

Diffusion of Fe through XG/$FeCl_2$ particles was about 2 to 5 orders of magnitude less than O_3 and had a range of about 5 orders of magnitude from dry to $RH = 80\%$. We note that we have not reported on self-diffusion coefficients of XG in aqueous solution, but it can be found in previous literature[85] for a 10 g L^{-1} solution attaining 10^{-8} cm^2 s^{-1} which is about 3 orders of magnitude less than $D^{\circ}_{O_3}$ or D°_{Fe}. A caveat of our analysis is that Fe^{2+} may complex with XG[80,86] and therefore, D_{Fe} may be considered an apparent diffusion of free ions and those in complex which may have higher and lower diffusion coefficient values, respectively.

In dry XG/$FeCl_2$ particles, H_{O_3} was 3 orders of magnitude higher than for pure water. Greater solubility of O_3 in organic liquids compared to water is well known[36,47,87] and can be explained by a "salting-in" effect. This is characterized by an increase in the product of ionic strength and activity coefficients of the solution (i.e. decreasing water content) and thus causes an increase in gas solubility. We note that a similar result is found for O_2 solubility, which is generally higher in organic liquids than in water[88,89]. The degree to which activity of XG/$FeCl_2$ solutions changes as a function of RH is not known. Therefore, we use again a Vignes-type equation as a function of water mole fraction (eqn (7)) to parameterize the RH dependence of H_{O_3} shown in Fig. 4. A mixing rule was also derived for comparison following

$$\log H_{O_3} = wt_w \log H^{\circ}_{O_3} + (1 - wt_w) \log H_{O_3}(RH = 0\%), \quad (9)$$

where wt_w is the weight fraction of water in the particles. Equation (9) is also shown in Fig. 4 and

determined without any fitting parameters since $H^{\circ}_{O_3}$ is taken from previous literature[47,79] and H_{O_3} at $RH = 0\%$ was experimentally derived. We find that eqn (7) is a better representation and recommended for use to describe O_3 solubility in XG. Clearly, eqn (9) does not agree with derived H_{O_3} parameters. Polymer chains in XG can overlap, aggregate and cross-link[85] giving rise to anomalous behavior of XG and oxygen diffusion in aqueous XG solution[85,90]. It may be possible that our ternary XG-$FeCl_2$-water system is non-ideal and deviates from ideal mixing. To our knowledge, this is the first report of O_3 solubility in XG. We suggest further measurements should be done in dilute and concentrated XG solutions to understand these trends with RH and water content.

The sensitivity of parameters D_{O_3}, D_{Fe} and H_{O_3} was tested to evaluate how unique they were at reproducing observed gradients. The parameters were fitted to minimize the sum of the squared residual values (RSS) between observed and modeled 2-D α profiles in Fig. 3. We were able to derive model sensitivity by changing one parameter at a time orders of magnitude and recalculating RSS. The percent change, ΔRSS/RSS, is shown in Fig. S8 of the ESI† as a function of all three parameter values and at all RH. In almost all cases, a single minimum in RSS was found demonstrating that diffusion and solubility parameters were unique when all other kinetic parameters were constrained. The range at which the RSS changed by dRSS/RSS=20% is shown as error bars in Fig. 4 following previous work[47]. For the case of RH=00%, a lower sensitivity range for D_{O_3} and H_{O_3} was found, however, an upper range could not be calculated due to numerical error that arose explained in detail in the ESI†. Briefly, KM-SUB defines a static set of spherical shells or layers. Raising O_3 diffusion or solubility significantly higher than its fitted value at $RH = 0\%$ caused significant penetration into the particle bulk requiring thousands of layers or more to resolve its concentration gradient, which we could not computationally afford. In order to reduce the total number of layers for efficient calculation, dynamic (changing in time) layer splitting and merging should be applied to have more layers for closely spaced concentration gradients and less layers for essentially uniform gradients. To constrain the sensitivity of D_{O_3} for $RH = 0\%$, we use the value from $RH = 20\%$. Due to most model sensitivity appearing symmetric, we choose a symmetric sensitivity range for H_{O_3}.

Figure 5 shows 3-D profiles of α and $[O_3]$ normalized to its maximum concentration, $[O_3]_{max}$, at each RH derived from the KM-SUB model. Values of $[O_3]_{max}$ are given in Table 1. The 3-D profiles of α in Fig. 5 are exactly the 2-D derived profiles seen in Fig. 3 (solid lines). Gradients in α at $RH = 0\%$ (Fig.

5a) spanned a few nanometers. A reduction in gradients to roughly a uniform profile over hundreds on nanometers was determined as RH increased to 80% as seen in Fig. 5i. Despite the extent of gradients in α, O_3 was found only in the first picometer to 2.7 nm at $RH = 0$ to 80%, respectively. We note that a length of 1 pm is much smaller than molecular scale and the Fe^{2+} ionic diameter of 0.7 Å. However, constraining layer thickness to 0.3nm as previously done[47] could not resolve O_3 gradients in our case. We therefore can only define layer thickness to satisfy continuum condition, meaning that we allowed layer thickness without a lower limit. We argue that this has no consequence, however, because bulk diffusion follows Fick's Law treating an ensemble of molecules. In general, oxidation reactions must have only taken place where O_3 was, and so gradients in α extending far past O_3 penetration depths to nanometers and hundreds of nanometers must have been the result primarily of Fe diffusion.

3.5 A Case for Using a Reacto-Diffusive Framework

Our observations allowed us to test the most basic of assumptions for predicting α, that our particles were well-mixed for both Fe^{2+} and Fe^{3+} and also for O_2 and O_3 in equilibrium with Henry's Law. Oxidation of Fe^{2+} due to O_2 exposure follows the reaction

$$Fe^{2+} + O_2 \longrightarrow Fe^{3+} + O_2^{\cdot -}, \tag{R4}$$

where $k_{\mathrm{R4}} = 0.3\ \mathrm{M^{-1}\ s^{-1}}$ taken from previous literature[91,92]. Assuming that Henry's Law constant for O_2 in water, $H^{\circ}_{O_2} = 1.3 \times 10^{-8}$ M Pa^{-1} [93], applies to our XG/$FeCl_2$ with a O_2 partial pressure of 3000 Pa (for the PolLux environmental microreactor at a total pressure of 150 mbar), the equilibrium condensed phase O_2 concentration, $[O_2]$, would be 3.9×10^{-5} M. Then, the first order loss rate for Fe^{2+}, k^I, in reaction R4 is $k^I_{\mathrm{R4}} = 1.2 \times 10^{-5}\ \mathrm{s^{-1}}$. We compare this to $k^I_{R3} = 1.6 \times 10^{-2}\ \mathrm{s^{-1}}$ calculated using $H^{\circ}_{O_3}$ for water[93] and $[O_3]_g = 150$ ppb or 0.015 Pa partial pressure. Since k^I_{R3} is 3 orders of magnitude larger than k^I_{R4}, it comes to no surprise that to achieve a similar decay of α due to O_3 observed over hours, an experiment with only O_2 would need to last thousands of hours longer. This is consistent with our finding that O_2 reaction in our system is negligible. Applying $k^I_{\mathrm{R4}} = 1.2 \times 10^{-5}\ \mathrm{s^{-1}}$, we calculate the loss of $\alpha = \alpha_0 \exp(k^I_{\mathrm{R4}} t)$. After $t = 4$ hr, α would be depleted by 15%. Using k^I_{R3}, α would be 100% depleted over 4 hr. Clearly, this is in stark disagreement with our observations. If XG acted as

a ligand for Fe^{2+}, this may change the rate of reaction however whether reaction rates are enhanced or reduced may depend on the specific system involved. A previous study[91] found that rate coefficients of O_2 with a Fe^{2+}-fulvic acid complex was 100 M^{-1} s^{-1}, which is over 2 orders of magnitude greater than k^I_{R4}. Another previous study found that iron oxidation with OH, H_2O_2 and HO_2 was observed to be 3.4 times higher with humic acid ligands from waste water than without[94]. In contrast, it was found that iron in steel was complexed with XG in dilute solution and that oxidation and corrosion due to HCl was inhibited[86] implying a reduction in reaction rate. Due to a lack of observations of O_3 oxidation of xanthan gum ligands with Fe, we maintain our choice of k_{R3}, and argue decreasing molecular diffusion of Fe and O_3 leads to a significant decrease in the loss rate of Fe^{2+} far less than what is expected when considering particles are well-mixed and in equilibrium with Henry's Law.

We to test the applicability of a reacto-diffusive framework described in Steimer *et al.*[36] to predict ozone diffusion and reaction into our particles. This is an analytical solution to the chemical loss as a function of t, in contrast to the application of KM-SUB to model molecular reaction and diffusion with numerous spherical shells, which is quite computationally expensive especially when using global optimization methods. In order to derive α for comparison with observations, we first define the net flux of O_3 in the gas phase into the condensed phase as

$$J_{\text{net}} = \frac{\gamma\omega}{4}[\text{O}_3]_{\text{g}}, \tag{10}$$

where γ is the reactive uptake coefficient and ω is the mean thermal velocity of O_3. It is important to note that eqn (10) is the net flux that results in a loss of gas phase O_3 because γ is defined as the probability that a molecular collision on an aerosol particle surface results in an irreversible loss from the gas phase. The first order loss rate of O_3 from the gas phase is then

$$\frac{d[\text{O}_3]_{\text{g}}}{dt} = -\frac{\gamma\omega}{4}[\text{O}_3]_{\text{g}} N_{\text{p}} S_{\text{p}}, \tag{11}$$

where N_{p} is the number of particles per volume of air and S_{p} is the surface area of a single particle such that the product $N_{\text{p}}S_{\text{p}}$ is the total surface area of aerosol particles per volume of air. Implicit to eqn

(10) and (11) is that net O_3 loss in the gas phase equals to the Fe^{2+} loss or

$$\frac{d[Fe^{2+}]_g}{dt} = \frac{d[O_3]_g}{dt}, \tag{12}$$

where $[Fe^{2+}]_g$ is exactly the number of Fe^{2+} atoms in the particle phase per unit volume of air. Typically, $[Fe^{2+}]_g$ is not considered and so a conversion to the more familiar particle phase concentration is as follows,

$$[Fe^{2+}]_g = [Fe^{2+}] N_p V_p, \tag{13}$$

where $[Fe^{2+}]$ is previously defined as the number of Fe^{2+} atoms in the particle phase per unit volume of particle phase and V_p is the volume of a single particle such that the product $N_p V_p$ is the total volume of aerosol particles per volume of air. Substituting eqn (12) and (13) into eqn (11) yields

$$\frac{d[Fe^{2+}]}{dt} = -\frac{\gamma\omega}{4}[O_3]_g \frac{S_p}{V_p}. \tag{14}$$

Notice in Fig. 5 that the reaction of O_3 occurs in a thin shell below the surface. Therefore we follow the rate limiting case described in Worsnop *et al.*[95] that the uptake of O_3 is controlled by a fast reaction within the reacto-diffusive length much smaller than the particle radius. Following Worsnop *et al.*[95] and Hanson and Lovejoy[96]

$$\gamma = \frac{4H_{O_3}RT_p}{\omega}\sqrt{D_{O_3}k_{R3}[Fe^{2+}]}, \tag{15}$$

where R is the universal gas constant. When substituting in eqn (15) into (14), the square-root dependence on the depletion of Fe^{2+} in a particle can be written as

$$\frac{d[Fe^{2+}]}{dt} = -k^D\sqrt{[Fe^{2+}]}, \tag{16}$$

where

$$k^D = -H_{O_3}[O_3]_g RT_p \sqrt{D_{O_3}k_{R3}}\frac{6}{d_p}, \tag{17}$$

is the equation for the reacto-diffusive rate constant[36]. We note that S_p/V_p of half spheres on a flat

plate is $6/d_\mathrm{p}$. Solving eqn (16) and substituting in eqn (17) and α from eqn (1) yields,

$$2\left(\sqrt{\alpha}-\sqrt{\alpha_\circ}\right)=-H_{\mathrm{O_3}}RT_\mathrm{p}\sqrt{\frac{D_{\mathrm{O_3}}k_{R3}}{[\mathrm{Fe_{tot}}]}}\frac{6}{d_\mathrm{p}}\int_0^t[\mathrm{O_3}]_\mathrm{g}\,dt. \tag{18}$$

Rearranging eqn (18) and again recognizing that $\chi(t)=\int_0^t[\mathrm{O_3}]_\mathrm{g}\,dt$ results in the following relationship,

$$\frac{d_\mathrm{p}}{3RT_\mathrm{p}}\frac{[\mathrm{Fe_{tot}}]\left(\sqrt{\alpha}-\sqrt{\alpha_\circ}\right)}{\chi(t)\sqrt{k_{R3}}}=H_{\mathrm{O_3}}\sqrt{D_{\mathrm{O_3}}}. \tag{19}$$

The left hand side of eqn (19) is entirely dependent on measurable and available quantities while the right hand side is in terms of the fitted parameters used in KM-SUB. Therefore, this provides a point of comparison to evaluate the suitability of the reacto-diffusive framework to predict Fe oxidation reaction. Equation (19) is applied to each individual particle probed. Figure 6 shows a box plot of experimentally derived and fitted $H_{\mathrm{O_3}}\sqrt{D_{\mathrm{O_3}}}$ as a function of RH. The 25 and 75 percentiles of $H_{\mathrm{O_3}}\sqrt{D_{\mathrm{O_3}}}$ data capture well the values of the fitting parameters from KM-SUB (Table 1). Median values are indicated by a horizontal solid line within the boxes. It is important to note that for some particles mainly those investigated within minutes of the start of reaction, depletion of α is small and scatters around $\alpha_\circ$. This leads to negative values of $\sqrt{\alpha}-\sqrt{\alpha_\circ}$ and thus negative values of $H_{\mathrm{O_3}}\sqrt{D_{\mathrm{O_3}}}$, which is physically unrealistic. However, we choose to include these in Fig. S9 as they contribute to the scatter in our data. If a data point falls outside of three times the average deviation from the median, it is considered an outlier and shown as a symbol with a cross in Fig. S9.

Direct comparison of data and model (eqn (19)) validate the use of the reacto-diffusive framework. An important feature of eqns (16) and (17) is that D_Fe is not required, which inherently means that the reacto-diffusive framework assumes uniform gradients in α. Despite observed reaction gradients (Fig. 3), the assumption that $\mathrm{Fe^{2+}}$ was well-mixed is "good enough" due to agreement in Fig. 6. We rearrange eqn (19) and use the quartile range of $H_{\mathrm{O_3}}\sqrt{D_{\mathrm{O_3}}}$ to calculate $\alpha(t)$ following

$$\alpha(t)=\left(\sqrt{\alpha_\circ}-\frac{3\left(H_{\mathrm{O_3}}\sqrt{D_{\mathrm{O_3}}}\right)RT_\mathrm{p}\sqrt{k_{R3}}\chi(t)}{\sqrt{[\mathrm{Fe_{tot}}]}d_\mathrm{p}}\right)^2, \tag{20}$$

without any input from KM-SUB. Figure 2 shows the result as a shading using the geometric mean of

d_p respective to each experiment. There is good agreement between data and predictions considering all uncertainties. The vast number of particles and the high time resolution used in our observation ensures enough data is available to effectively conclude that approximation in the reacto-diffusive framework is acceptable to describe O_3 oxidation.

We previously noted that model predicted 3-D profiles in α were much sharper than those in 2-D, which calls into question whether our 2-D observations were sensitive enough to quantify gradients at all. At $RH = 60\%$ for example, α dropped by ~ 0.5 over a 500 nm particle radius in 3-D after 1 hr of reaction. The conversion to 2-D profiles yielded a drop in α by ~ 0.2 for the same length scale. Despite the integration, however, 2-D profiles are highly sensitive to changes in 3-D as described in the ESI†, Fig. S10. Hypothetically speaking, depletion over t from $\alpha = 0.9$ to 0.5 could potentially look completely uniform with $\alpha = 0.5$ throughout the entire volume or completely inhomogeneous with 2 spherical shell regions having $\alpha = 0$ in the outer shell and 0.9 in the inner shell as seen in Fig. S10. If this occurred, we would have observed $\alpha = 0$ at the perimeter of particles and 5 pixels into the interior. This degree of homo- or inhomogeneity was never observed, and instead was always in between this extreme case and uniformity. We note that a spatial inversion of our data was not performed, i.e. from observed 2-D column integrated profiles to 3-D radial profiles. This would require data smoothing, constrained values or use of assumed functional forms because error and data scatter in inverting 2-D to 3-D profiles would propagate cumulatively from the exterior to the interior of particles potentially growing to infinity. Typically, a model that predicts observed uptake of gas phase oxidant, i.e. γ, and loss of condensed phase reactant or product production also derives aerosol internal composition. Unfortunately, gas phase loss of O_3 to aerosol surfaces or uptake coefficients could not be measured with our current setup and is instead calculated from KM-SUB given in the ESI†, Fig. S11. We suggest that measuring changes in internal chemical aerosol and gas phase composition not only in the particle bulk, but also with nanometer and sub-nanometer resolution, should be used to verify heterogeneous reaction processes which we were not sensitive to in this study such as a surface reaction, surface saturation, a second-order loss process on the surface, and surface self-reaction. In any case, we conclude that our 2-D profiles were an exact constraint on predicted 3-D profiles of where Fe and O_3 diffused and reacted yielding unique diffusion coefficients and Henry's Law constants.

We argue that a reacto-diffusive framework can apply to O_2 as it does for O_3. We observed no loss

of Fe^{2+} during O_2 exposure over hours, but calculated a 15% loss assuming particles were in equilibrium with Henry's law. Our uncertainty is small enough that if a 15% loss did occur, it would have been observed. Since it was not, we can claim that a reacto-diffusive framework also applied to O_2 and Fe^{2+}. This also implied that O_2 was limited to a thin surface layer and not found homogeneously in the particle bulk. Diffusion of O_2 may not be so different compared to O_3 following the Stokes-Einstein relation where the diffusion coefficient is inversely proportional to molecular radius[81,82] or equivalently, inversely proportional to the cubed root of molar mass ignoring solvation effects[97]. However, there may be inaccuracies when applying the Stokes-Einstein relation particularly at low RH and for small molecules diffusing through concentrated organic solutions with high organic molar mass[84]. Time scales of days would be required to study O_2 diffusion and reaction in this system which are impractical for STXM/NEXAFS experiments at a synchrotron light source.

Our findings that O_3 reaction follows the reacto-diffusive framework led us to speculate that other condensed phase reactions involving organic species can also be slowed due to a low diffusion. There is increasing evidence that predicting secondary organic aerosol (SOA) mass must take into account condensed phase chemical reactions that include in part, oligomerization or acid catalyzed and accretion reactions that significantly increase molecular weight, reduce re-evaporation of organic compounds to the gas phase and thus add to the total mass of SOA[20,98–100]. Examples of these are glyoxal uptake and reaction, oligomerization of volatile condensed phase molecules, aldol condensation and esterification[17,101–103]. Isoprene epoxydiols (IEPOX) are major gas phase products of isoprene oxidation that are highly soluble and reactive in the condensed phase[20,100]. When depleted in the condensed phase due to chemical reaction there, a net reactive uptake of IEPOX has been shown to lead to increasing organic and organosulfate formation contributing significantly to aqueous SOA mass in atmospheric environments[104]. However, Zhang *et al.*[105] showed in a laboratory study that when organic coatings were present on acidic aerosol particles, IEPOX reactive uptake decreased as coating thicknesses increased up to 32 nm and when RH was lowered from $50 - 15\%$. We speculate that irreversible uptake of IEPOX may also follow a reacto-diffusive framework. In general, diffusion limitations slow reactions compared to predictions considering homogeneous mixing and equilibrium with Henry's Law. For this reason, we suggest that aerosol chemical studies should be evaluated with the reacto-diffusive framework described here and in previous work[36,95,96] to test its predictive capability under a range of atmospheric condi-

tions. We call for a database of diffusion coefficients and Henry's Law constants applicable for oxidants in highly concentrated aerosol particles[84]. This would preferably be for a wide range of temperature and humidity and for materials such as secondary organic aerosol and their proxies[13]. Doing so would allow further evaluation of when the reacto-diffusive framework is a valid approximation to describe the loss of condensed phase reactants. We suggest that the reacto-diffusive framework may be pervasive to gas-to-particle kinetics which would certainly simplify representation of atmospheric heterogeneous chemistry.

4 Conclusions

We have measured concentration gradients within individual aerosol particles containing xanthan gum and $FeCl_2$ due to heterogeneous reaction with O_3. Oxidation from Fe^{2+} to Fe^{3+} was imaged in 2-D using STXM/NEXAFS prior and during *in situ* O_3 exposure for hours. Using a unique 2-D concentric perimeter analysis and careful error propagation, we were able to derive 2-D reaction profiles with well-defined uncertainties. Thousands of particles were probed, each with hundreds of pixels that provided quantitative spatial and chemical information about the reaction with O_3. We found that during O_3 exposure, increased oxidation occurred with increasing RH and $[O_3]_g$. At all reaction time and at particle perimeters, i.e. the outer most pixels of all particles, α was consistently lower than concentric pixels toward the particle center. Therefore, we conclude that O_3 oxidized particle surfaces more than interiors. Observed 2-D gradients in α from perimeter to center were shallow and ranged roughly by about 0.2 over the first 200 nm at $RH = 0$ and 22%. At $RH = 43$, 60 and 80%, a difference of 0.2 in α occurred for ≥ 500 nm. We conclude that changes in diffusion of O_3 and Fe must have occurred and were driven by the water content in xanthan gum, which is known to increase with increasing RH. To test this conclusion, we used the kinetic multi-layer model for aerosol surface and bulk chemistry, KM-SUB. Using previous literature values where possible and fitting parameters for diffusion coefficients of O_3 and Fe^{2+}, as well as Henry's Law constants for O_3 as a function of RH, we were able to predict 2-D concentration profiles. This is the first time that a direct comparison between observed and predicted internal aerosol spatio-chemical changes has been achieved. Resulting diffusion coefficients increased exponentially as a function of RH and was parameterized using a Vignes-type equation. H_{O_3} decreased

exponentially as a function of RH and could also be described using a Vignes-type equation. A volume mixing rule over-predicted H_{O_3} and is advised not to be used for this system. Our findings may apply for ozone in marine derived organic aerosol due to XG being a proxy of polysaccharide and exopolymer particles found to be aerosolized from oceans.

We have used a limiting case in heterogeneous aerosol chemistry referred to as a reacto-diffusive limitation to describe our results following a square root dependent loss rate of α. This corresponding framework assumes that a reactant is uniformly distributed (or well-mixed) and oxidation takes place in a thin layer at the aerosol surface. However, this is an approximation by definition and shallow gradients in Fe^{2+} were in fact, observed. To test appropriateness of this approximation, we used observed values only to derive the product of the Henry's Law constant and the square root of the diffusion coefficient for O_3, or $H_{O_3}\sqrt{D_{O_3}}$, at all experimental conditions. This product could be directly compared with those derived from KM-SUB. It was found that within experimental uncertainties, total depletion of Fe^{2+} could be reproduced for all experiments, and we conclude that for gradients observed here, the reacto-diffusive framework is applicable. This approximation makes predicting the loss rate of aerosol components significantly easier with no computational expense compared to the KM-SUB or any other multilayer reaction and diffusion models. Furthermore, important chemical and physical parameters in the reacto-diffusive framework such as diffusion coefficients, Henry's Law constants, and second order bulk reaction rates are currently capable of being derived in a laboratory setting or a controlled setting in the ambient atmosphere. We have derived these parameters for O_3 in xanthan gum as a proxy for a natural biogenic source of organic matter emitted directly into the marine atmosphere. Their use should give better representation of condensed phase loss and production rates of reactants and products in marine aerosol with O_3. Furthermore, we also suggest that the reacto-diffusive framework should be evaluated for various oxidants and reactants under a wide range of temperature and humidity to further validate its use in atmospheric heterogeneous chemical reactions.

5 Methods

Mixed XG and $FeCl_2$ particles were nebulized from dilute aqueous solution, dried and impacted onto silicon nitride membranes. The carbon to iron atomic ratio was 3.5 to 1 assuming a XG monomer

of $C_{35}H_{49}O_{29}$ at 933.76 g mol^{-1}. Prior to impaction, silicon nitride substrates were pre-glued into removable sample exchange clips fitted to either of two microreactors named, the PolLux environmental microreactor[106] and the MPI-C aerosol micro-reactor[107]. Both allowed particles to be exposed to He, O_2, H_2O and O_3 at a desired partial pressure and $T_p = 20°$ C, and thus RH and reactive gas exposure could be well-controlled[36,106]. Both microreactors are described in detail elsewhere[106,107], and only specific operating conditions pertaining to our experiments are given here and in the ESI†. Helium was used as a carrier gas with a flow of 20 cm^3 min^{-1} at standard temperature and pressure (STP). A flow of O_2 at 5 cm^3 min^{-1} STP first passed through a custom built UV lamp O_3 generator then mixed with the humidified He flow. The concentration of O_3 over t is given in Fig. S5 of the ESI†. The calculated water partial pressure and T_p was used to determine the RH the particles were exposed to using the saturation vapor pressure parameterizations following Murphy and Koop[108]. A total cell pressure of 150 mbar and flow rate of 25 cm^3 min^{-1} was maintained. The operating principle of the MPI-C aerosol micro-reactor is similar to the PolLux microreactor. The MPI environmental cell was coupled to the same gas flow system as the PolLux microreactor with equal gas flow rates. However, the cell pressure was maintained at $\sim$ 450 mbar. This allowed for a greater concentration of O_2 in the O_3 generator, and thus a greater $[O_3]_g$ for experiment with higher exposure. Detailed experimental methods are further outlined in the ESI†.

The Fe oxidation state and carbon functionality was probed using STXM/NEXAFS at the PolLux endstation located at the Swiss Light Source (SLS)[109]. The transmission of X-ray photons through the particle was measured and converted to optical density, $OD = -\ln(I/I_0)$, where I_0 and I are the incident and transmitted photon count, respectively, and their uncertainty is $\sigma_{I_0} = \sqrt{I_0}$ and $\sigma_I = \sqrt{I}$. X-ray light was focused to a 35 by 35 nm spot size while scanning a field of view (FOV) on the order of micrometers to generate an OD image at a single X-ray energy. An image was made of hundreds to thousands of individually measured pixels, where each is the OD over an area of 10^{-3} μm^2. Multiple OD images over the same FOV taken over a range of X-ray energies were aligned and processed using publicly available software[110]. We primarily investigated the X-ray energy range 700-735 eV, which is the Fe L-edge absorption. When present in particles, peak absorption due to Fe^{2+} and Fe^{3+} occur at slightly different X-ray energies, allowing to differentiate between the two[111,112]. The X-ray energy at Fe^{2+} peak absorption for $FeCl_2$ measured here was compared with previous literature[57] and an energy

offset was obtained as a calibration. Peak absorptions for ferrous and ferric chloride are at 707.8 and 709.5 eV, respectively[57] as seen in Fig. 1.

The KM-SUB model was used to simulate chemical reaction and molecular diffusion inside of our XG/$FeCl_2$ particles and infer diffusion and solubility parameters[43,47]. A detailed description of KM-SUB can be found in Shiraiwa *et al.*[43] and Berkemeier *et al.*[47]. Briefly, this model solves the system of non-linear differential equations for the time rate of change of O_3 and Fe^{2+} in prescribed layers with defined thickness. It accounts for O_3 accommodation and absorption, the O_3 and Fe^{2+} transfer from the surface and within bulk layers and finally, the chemical loss of O_3 and Fe^{2+}. A single spherical aerosol particle geometry with $d_p = 0.5$ μm was applied for all simulations. The model had 2 spatial regions where the first extended from the surface to a short distance into the bulk and hosted 100 to 500 finely spaced layers to resolve the O_3 concentration there. The remaining particle bulk had evenly spaced layers with 0.5 to 2 nm thickness, which was sufficient to resolve observed Fe^{2+} gradients. The total number of layers in a simulation varied between 500-1500 depending on O_3 and Fe^{2+} gradients. Initial α was approximated to be uniform through the particle. γ was calculated using the O_3 surface coverage, the net flux from the gas phase and the collision flux[43,47]. The model was modified to include changing $[O_3]_g$ concentration over t. The Knudsen number for our flow conditions was on the order of 10^0 and γ was on the order of $10^{-4} - 10^{-6}$ during reaction. These were used to determine the gas diffusion correction factor[40] close to unity and thus could be ignored.

6 Conflict of Interest

We declare no conflict of interest.

7 Tables

Table 1: Parameters and their units used in the KM-SUB model.

		$RH = 0\%$	$RH = 22\%$	$RH = 43\%$	$RH = 60\%$	$RH = 80\%$
k_{R3}	$cm^3\ s^{-1}$			6.20×10^{-16}		
k_{slr1}	$cm^2\ s^{-1}$			6.27×10^{-14}		
k_{slr2}	$cm^2\ s^{-1}$			4.31×10^{-17}		
k_{bs,O_3}	$cm\ s^{-1}$	0.69	0.69	0.69	0.69	1.60
$k_{sb,Fe}$	s^{-1}	9.22×10^{-5}	3.34×10^{-4}	6.95×10^{-4}	8.83×10^{-4}	4.20×10^{-4}
D_{O_3}	$cm^2\ s^{-1}$	2.48×10^{-16}	1.48×10^{-15}	1.66×10^{-10}	3.50×10^{-10}	4.17×10^{-8}
D_{Fe}	$cm^2\ s^{-1}$	5.52×10^{-18}	2.84×10^{-15}	3.94×10^{-14}	1.46×10^{-13}	2.24×10^{-13}
H_{O_3}	$mol\ cm^{-3}\ atm^{-1}$	2.21×10^{-2}	4.80×10^{-3}	1.49×10^{-3}	5.87×10^{-4}	3.60×10^{-4}
α_0		0.90	0.86	0.83	0.70	0.90
K_{bs}	cm	2.41×10^{-9}	1.99×10^{-9}	2.21×10^{-9}	2.95×10^{-9}	5.82×10^{-9}
τ_{d,O_3}	s			5.32×10^{-4}		
$\alpha_{s,0}$				0.50		
σ_{Fe}	cm^2			2.19×10^{-16}		
$[Fe_{tot}]$	cm^{-3}	6.15×10^{21}	6.06×10^{21}	5.93×10^{21}	5.74×10^{21}	4.99×10^{21}
$[O_3]_{max}$	cm^{-3}	1.91×10^{16}	5.71×10^{15}	9.08×10^{13}	7.72×10^{14}	1.58×10^{13}
σ_{O_3}	cm^2			2.42×10^{-14}		
$D_{g,O3}$	$cm^2\ s^{-1}$			0.91		

Table 2: Fitting parameters for the Vignes-type equation (eqns (5)-(8)). The subscript "X" represents either O_3 or Fe.

	D°_X	$D_X(RH = 0\%)$	H°_X	$H_X(RH = 0\%)$	C	D
D_{O_3}	1.90×10^{-5} [a]	7.45×10^{-18}			1.73	-0.17
H_{O_3}			1.20×10^{-5} [b]	3.93×10^{-2}	1.21	-0.50
D_{Fe}	7.19×10^{-6} [c]	4.53×10^{-18}			0.67	-1.15

[a] Berkemeier *et al.* [47], Smith and Kay [79]
[b] Sander [93]
[c] Vanýsek [113]

8 Figures

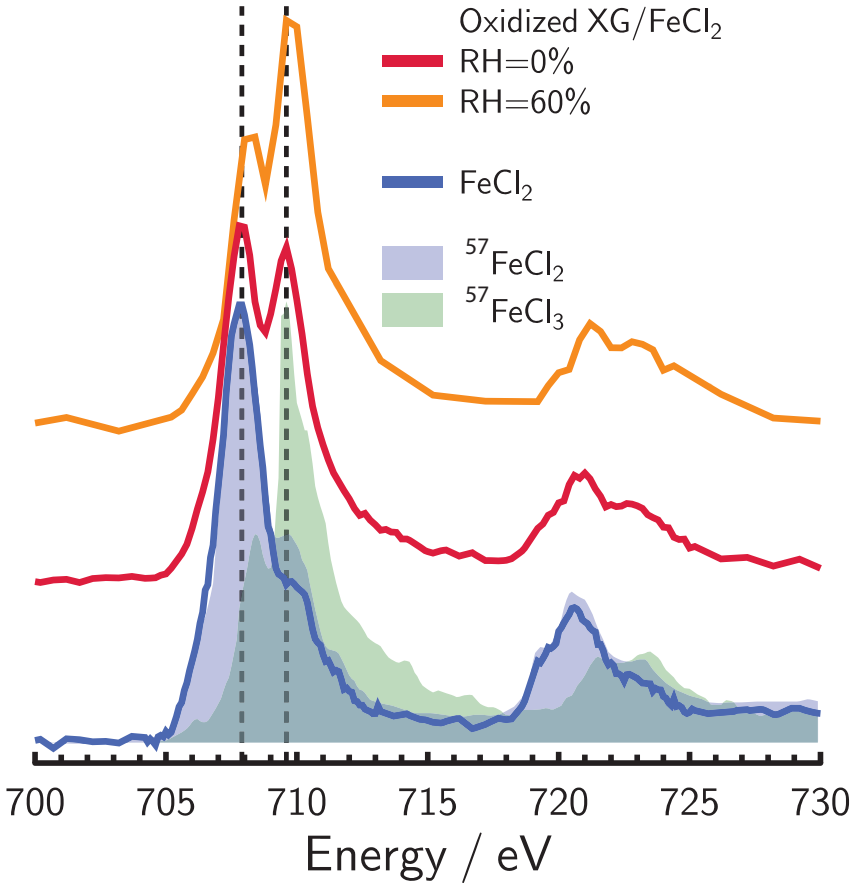

Figure 1: Near edge X-ray absorption fine structure (NEXAFS) spectra of oxidized XG/$FeCl_2$ particles at $RH = 0$ and 60% shown as the red and orange lines, respectively, along with measured $FeCl_2$ spectra as the blue line. Chemical standards for ferrous and ferric chloride are shown as the blue and green shading, respectively[57]. Spectra have been scaled and shifted vertically for clarity. Dashed lines indicate typical peak absorption for Fe^{2+} and Fe^{3+} at X-ray energies of 707.9 and 709.6 eV.

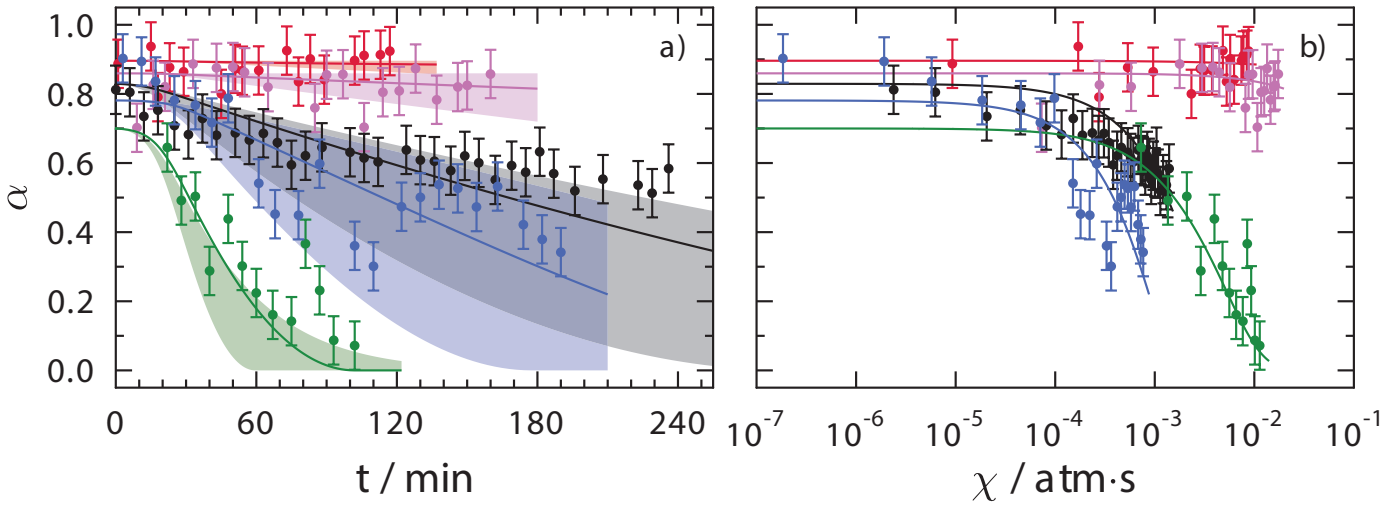

Figure 2: Measured and modeled depletion of the Fe^{2+} fraction, α, as a function of a) time, t, and b) ozone exposure, χ, for RH = 0, 22, 43, 60 and 80% as red, pink, black, green and blue circles, respectively. Each data point was determined from approximately 5-25 particles each within a field of view imaged with STXM. The error bars are either ± 0.07 or the propagated error from photon counting statistics, whichever is greater. Solid lines are calculations from the KM-SUB model using parameters given in Table 1. Shadings in panel a) are predictions applying the reacto-diffusive framework described in more detail in the text.

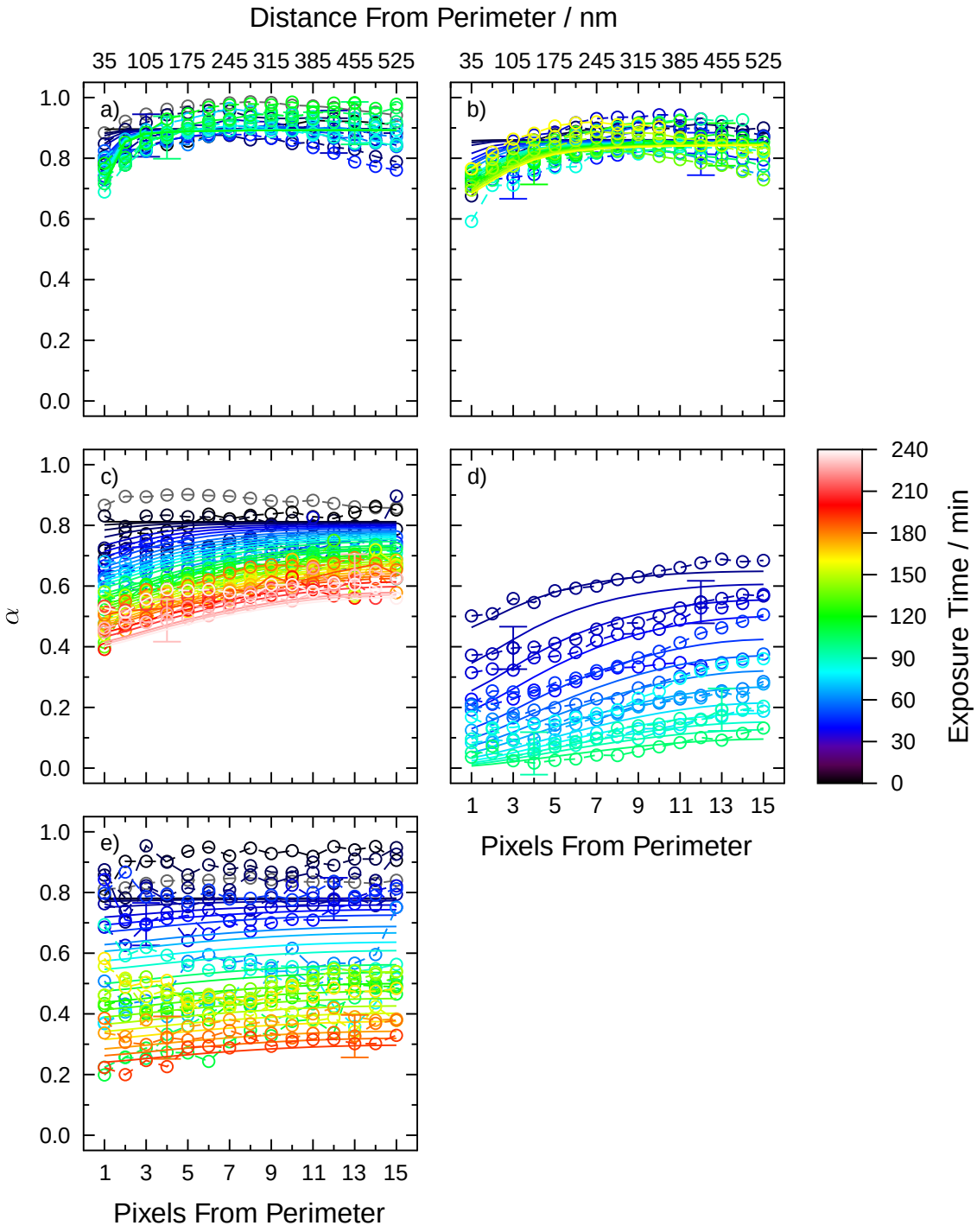

Figure 3: Observed and modeled 2-D profiles of the Fe^{2+} fraction, α, as a function of O_3 exposure time as the color scale at a *RH* of a) 0%, b) 22%, c) 43%, d) 60% and e) 80%. Grey symbols are initial conditions prior to O_3 exposure. Example error bars are included only on some data points for clarity. The bottom and top abscissa are the pixels and distance from the particle perimeter, respectively, where each pixel has a spatial dimension of 35 by 35 nm. Solid lines are fit to this data with parameters given in Table 1.

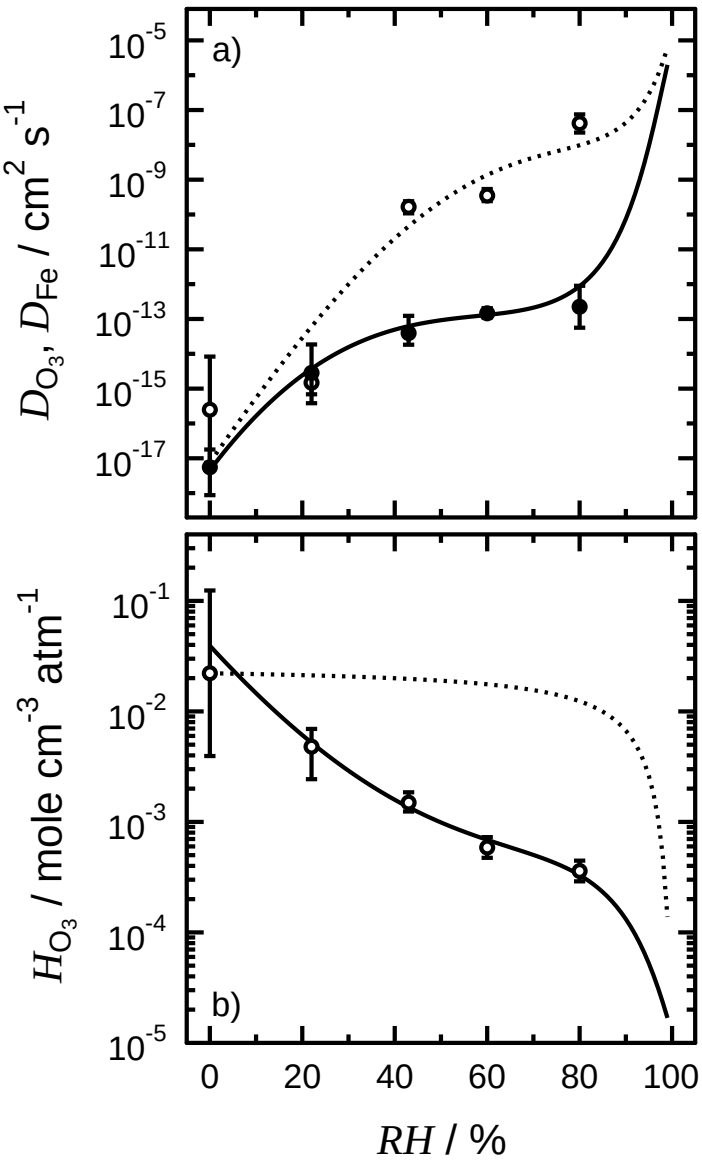

Figure 4: Fitted parameters from the KM-SUB model. a) The diffusion coefficient for O_3 (white circles), D_{O_3}, and the diffusion coefficient for Fe (solid symbols), D_{Fe}, are shown as a function of RH for mixed xanthan gum and $FeCl_2$ particles. A Vignes type parameterization for D_{O_3} and D_{Fe} are the dotted and solid lines, respectively. b) Henry's Law constant for O_3, H_{O_3}, as a function of RH is shown as white circles. Error bars indicate the fit sensitivity described in the text and the ESI†. The dotted and solid line is determined from a volume mixing rule and a Vignes type parameterization, respectively.

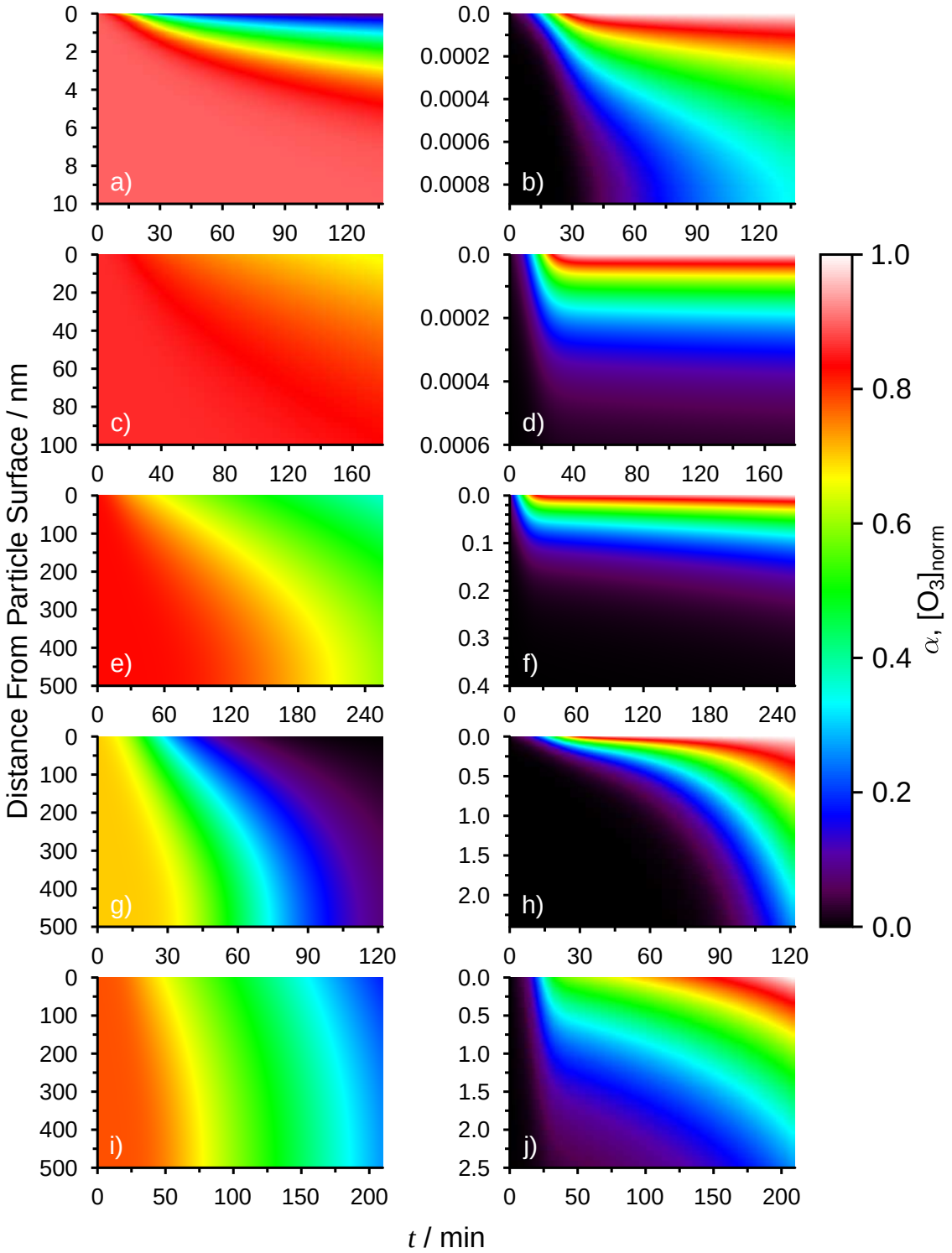

Figure 5: Model derived 3-D radial profiles of the Fe^{2+} fraction, α and normalized O_3 concentration, $[O_3]_{norm} = [O_3]/[O_3]_{max}$, where $[O_3]_{max}$ is the maximum O_3 concentration for $RH = 0\%$ (a-b), 22% (c-d), 43% (e-f), 60% (g-h) and 80% (i-j). The color scale from $0 - 1$ is the same for both α shown in the left panels (a, c, e, g and i) and $[O_3]_{norm}$ shown in the right panels (b, d, f, h and j). The distance from the particle surface is the ordinate. Note that the scales for all panels can be different.

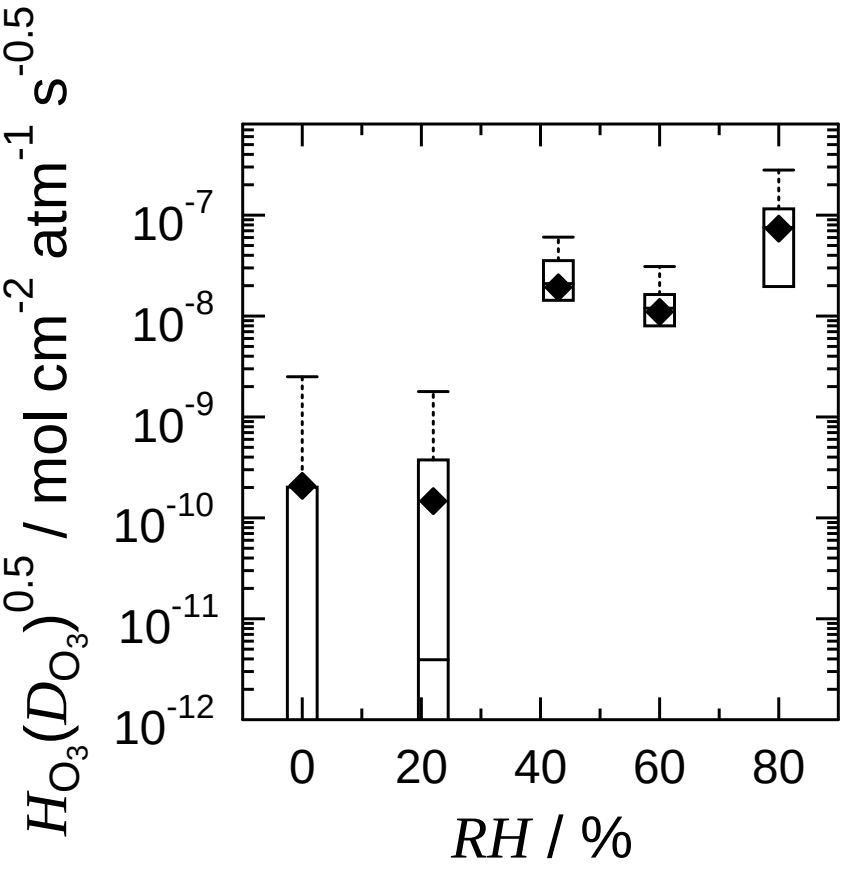

Figure 6: A box plot of the product of Henry's Law constant for ozone, H_{O_3}, and the square root of the diffusion coefficient of ozone, D_{O_3}, or $H_{O_3}\sqrt{D_{O_3}}$ as a function of RH. The bottom and top of the boxes represent 25 and 75 percentiles of about 1550 particles. Horizontal lines within boxes are median values. Upper error bars indicate 3x the average deviation of the median, however this extends to negative values thus lower error bars are not depicted. All data for individual particles is shown in Fig. S9. Solid diamonds are derived from fitted parameters in Table 1.

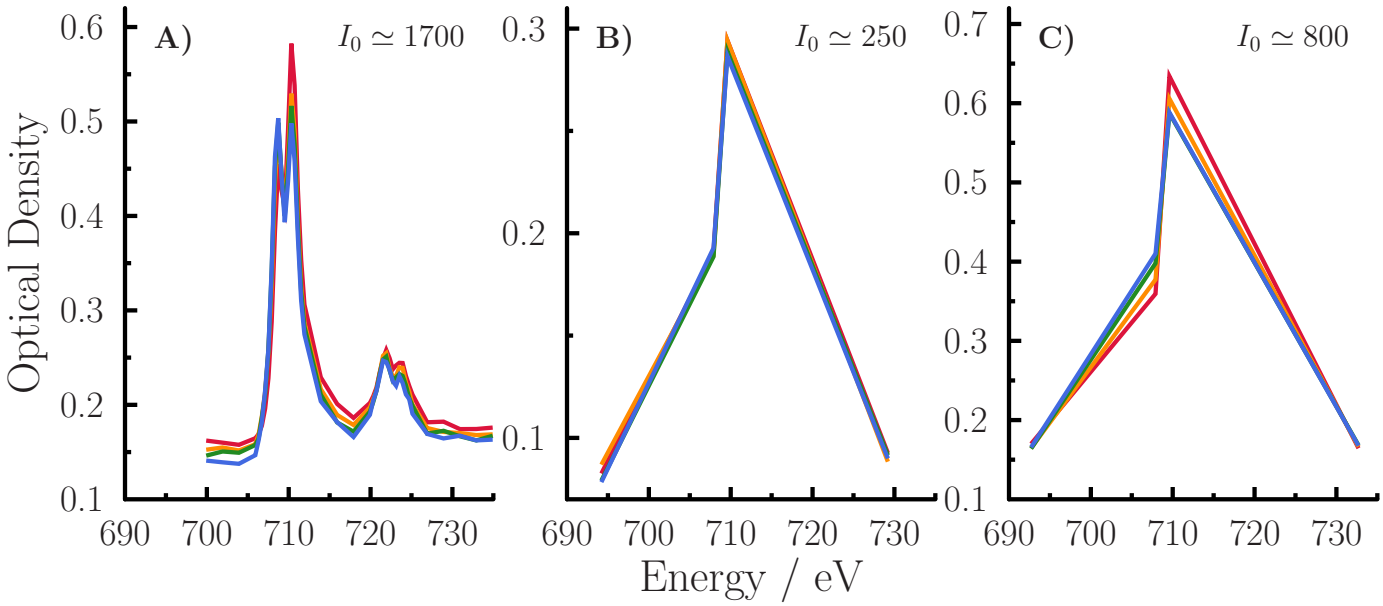

Figure S1: Damage assessment of X-ray exposed particles of xanthan gum (XG) mixed with $FeCl_2$. Blue, green, orange and red colors were acquired one after another and indicate increasing damage. a) A full near edge X-ray absorption fine structure (NEXAFS) spectra over the same particle is shown where each pixel was irradiated with approximately 1700 photons at 50 energy points. b) A map (4 energy points) of particles where each pixel was irradiated with approximately 250 photons. c) A map of particles where each pixel was irradiated with approximately 800 photons.

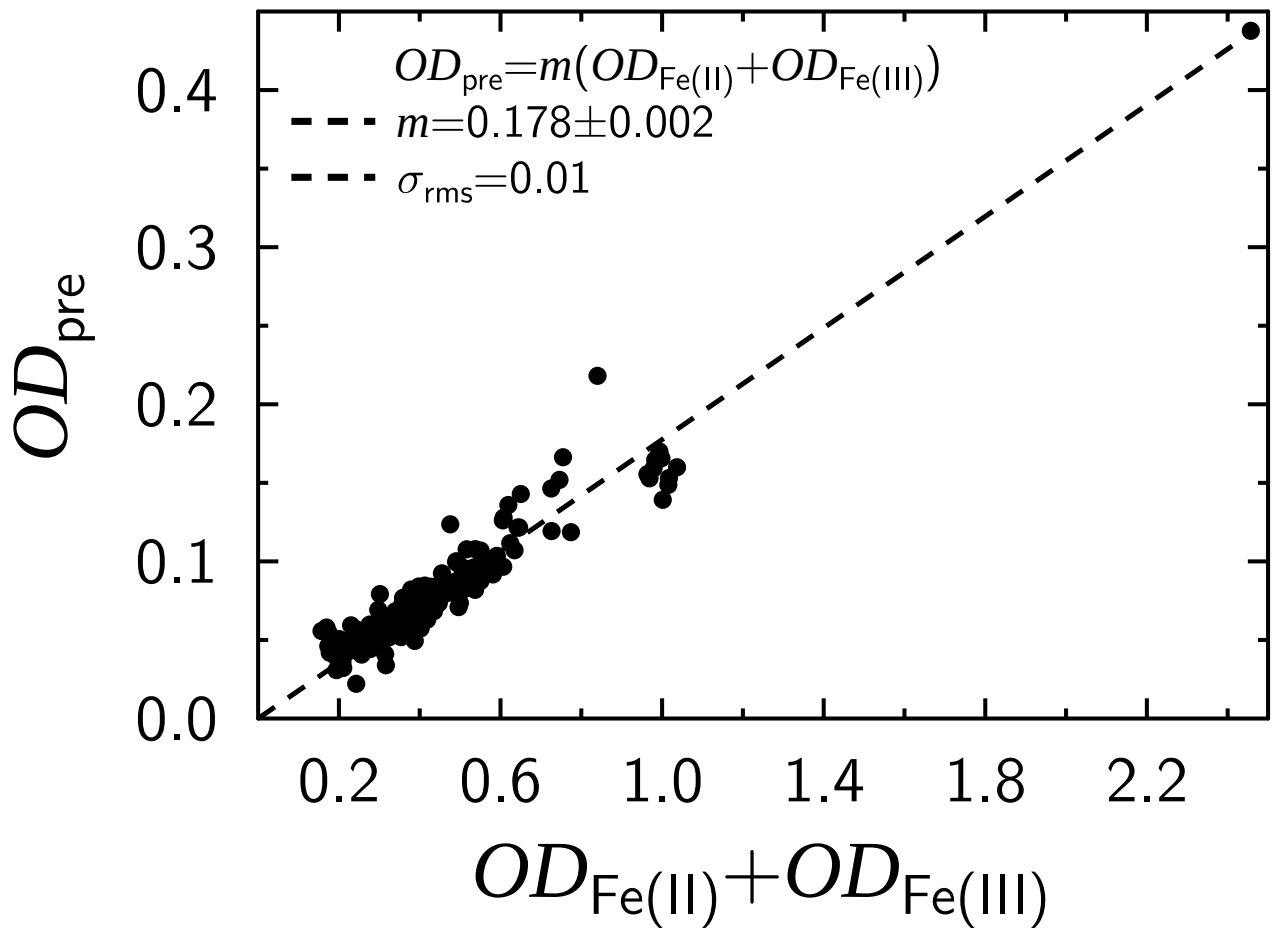

Figure S2: Average optical density derived at the Fe pre-edge, OD_{pre}, as a function of the sum of optical density at the Fe^{2+} and Fe^{3+} peak at 707.8 and 709.5 eV, respectively, or $OD_{\mathrm{Fe^{2+}}} + OD_{\mathrm{Fe^{3+}}}$. Each symbol is the average over an individual particle. The dashed line is a fit to the linear equation indicated in the figure.

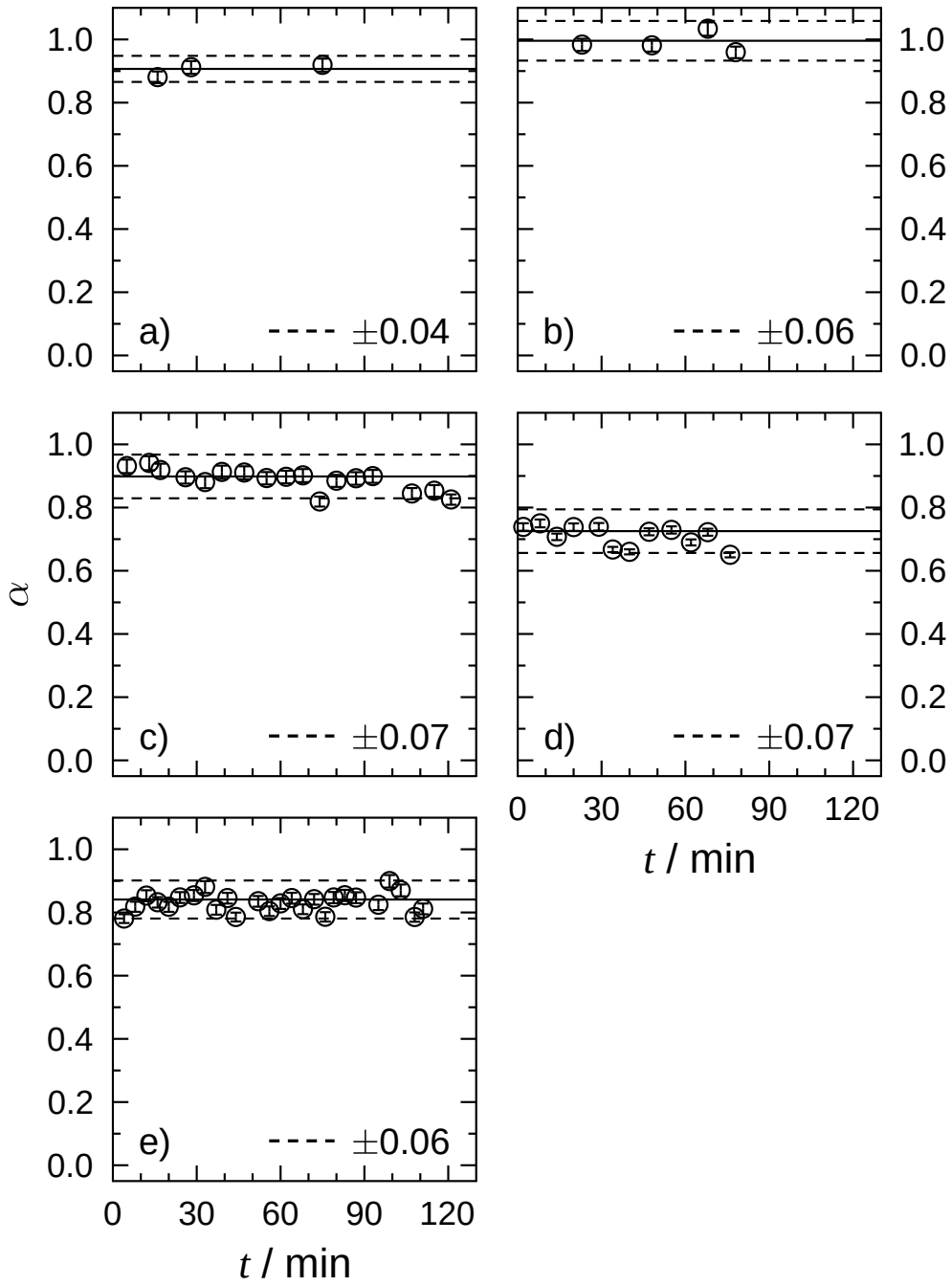

Figure S3: Measured Fe^{2+} fraction, α, as a function of time, t, during oxygen exposure for a) $RH = 0$, b) 22, c) 43, d) 60 and e) 80%. Each data point is determined from approximately 5-25 particles. The error bar indicates the error on the average value propagated from X-ray photon counting statistics. The solid line is the average value of individual particles from Fig. S4. The dotted lines are the standard deviation of α for individual particles shown in Fig. S4.

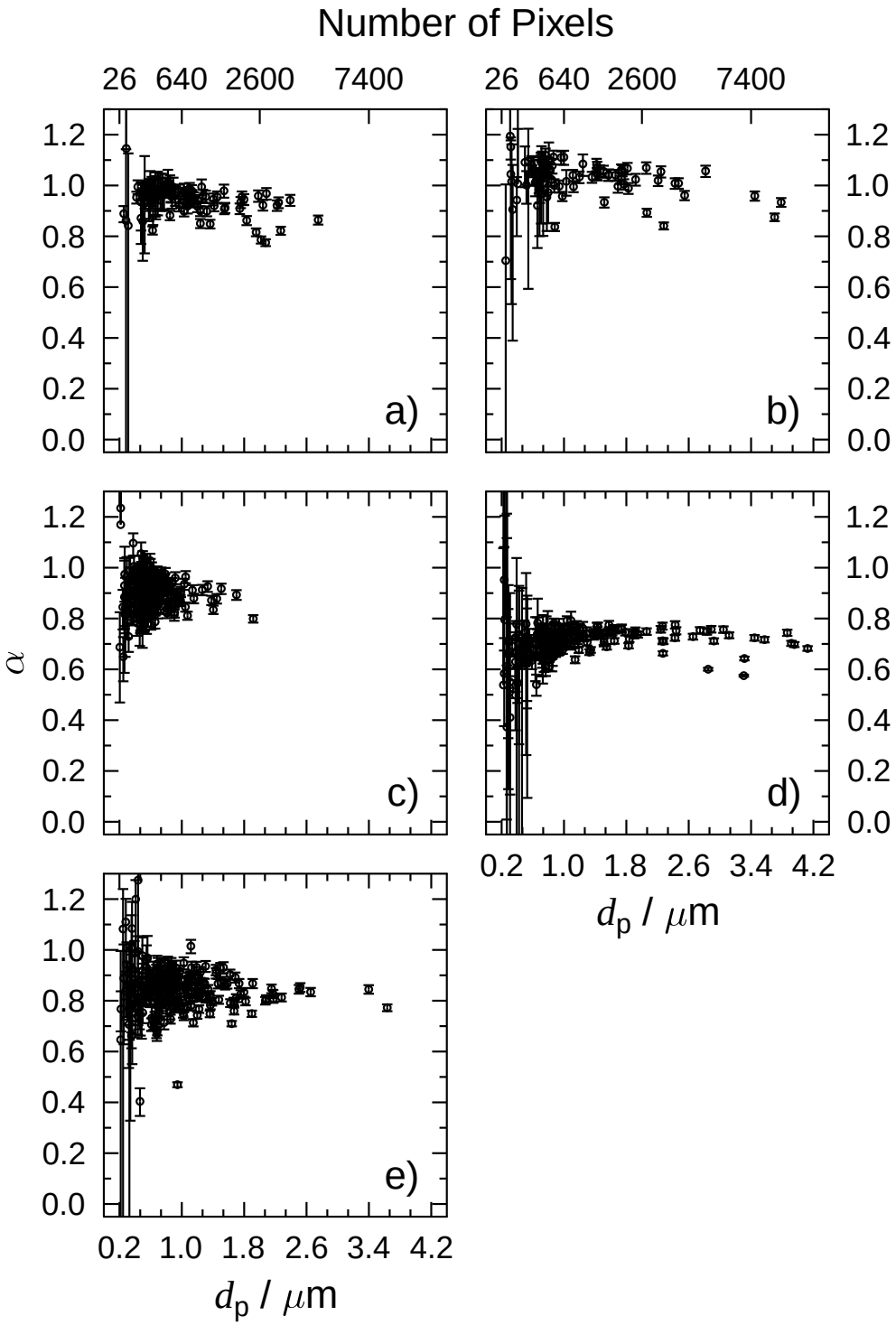

Figure S4: Measured Fe^{2+} fraction, α, as a function of particle diameter, d_p, during O_2 exposure for a) $RH = 0$, b) 22, c) 43, d) 60 and e) 80%. Each data point is an average over a single particle where the number of pixels per particle is given in the top abscissa. The data here was also used to determine averages in Fig. S3. Error bars indicate the error on the average value propagated from X-ray photon counting statistics. The standard deviation of α for individual particles is not shown here, but included in Fig. S3.

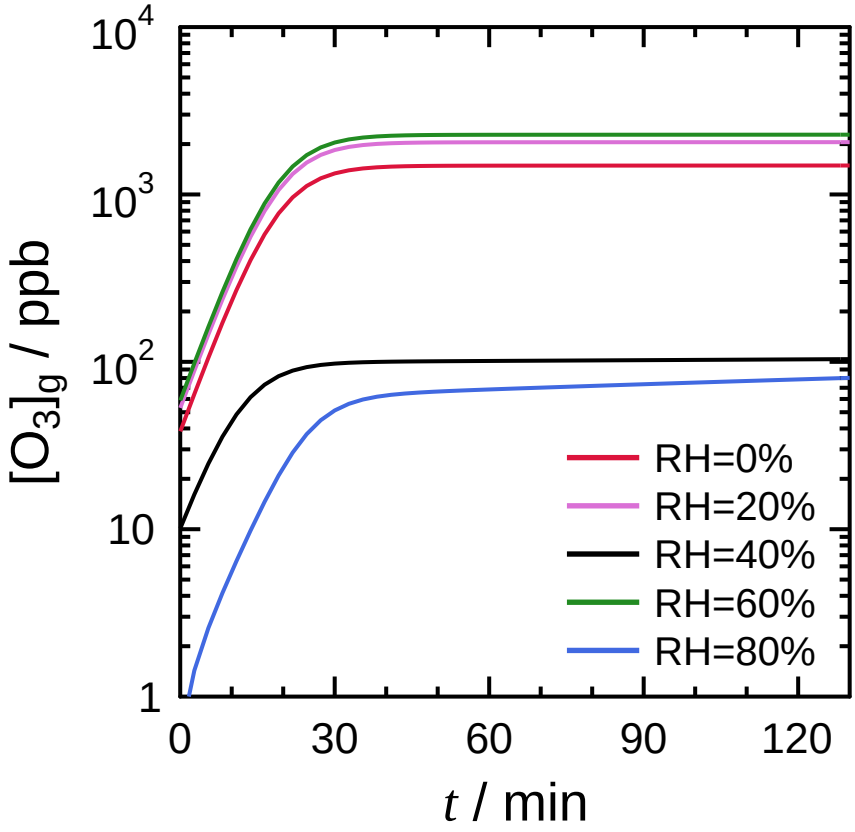

Figure S5: The observed gas phase ozone concentration, $[O_3]_g$, at standard temperature and pressure as continuous functions in time, t, for all experiments used the KM-SUB model. Relative humidity, RH, for each experiment is indicated.

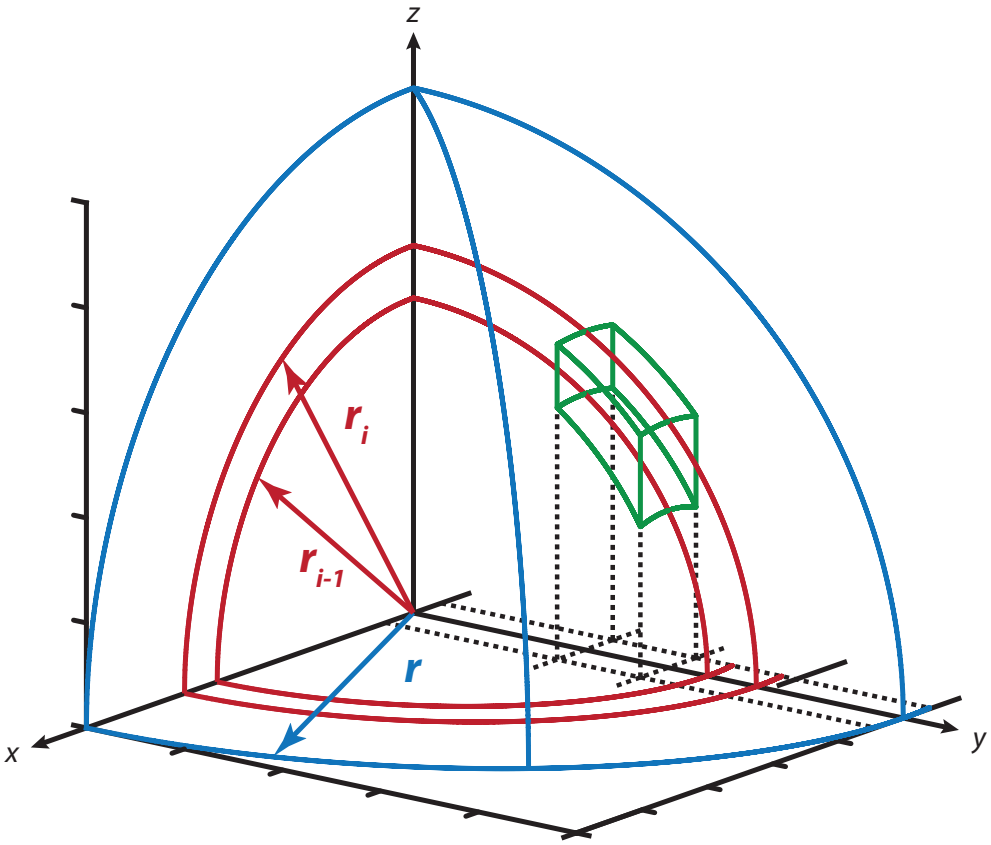

Figure S6: Geometric representation of a 2-D projection on a grid box of a finite volume from a spherical shell outlined in green inside of an spherical aerosol particle. The particle radius is r and outlined in blue. The shell outside and inside diameter is r_i and r_{i-1}, respectively, and outlined in red. Black solid lines are the axis and black dashed lines indicate the grid box.

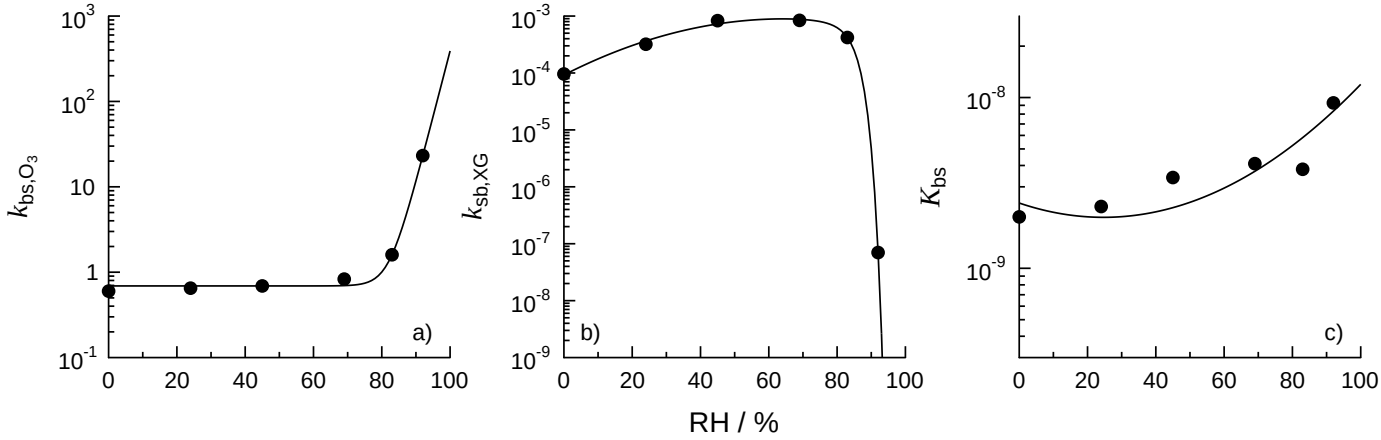

Figure S7: Relative humidity, RH, dependent parameters used in the KM-SUB model. These parameters are the bulk to surface transfer rate coefficient for O_3, $k_{\mathrm{bs,O_3}}$, the surface to bulk transfer rate coefficient, k_{sb}, and the surface equilibrium constant, K_{bs}. Symbols are taken from Berkemeier *et al.*[47] and solid lines are parameterizations as a function of RH.

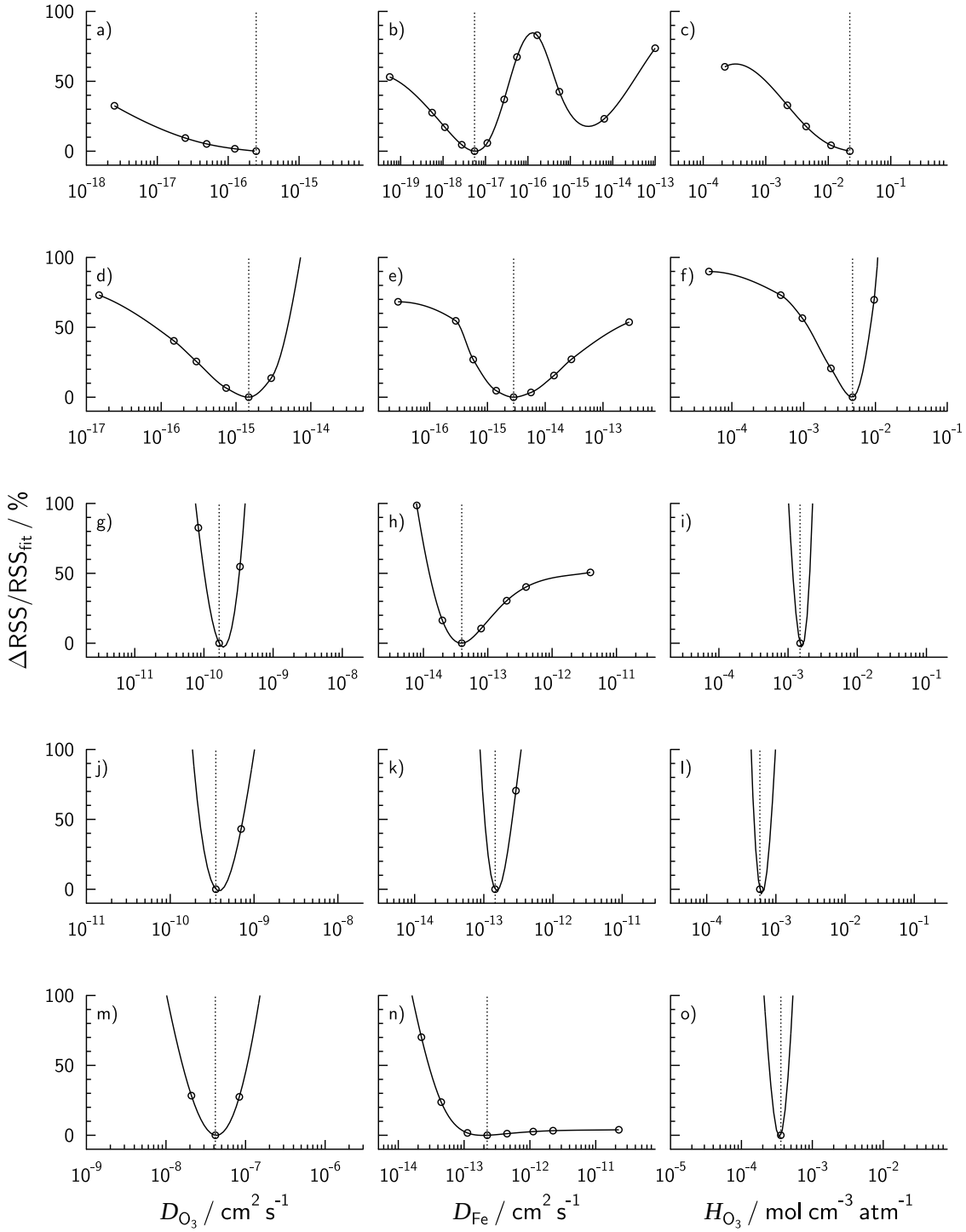

Figure S8: Model sensitivity on the fitted ozone diffusion coefficient, D_{O_3}, iron diffusion coefficient, D_{Fe}, and ozone Henry's Law constant, H_{O_3}, at (a-c) 0%, (d-f) 22%, (g-i) 43%, (j-l) 60% and (m-o) 80%. The percent change in the sum of the squared residual values (RSS) was determined as $\Delta RSS/RSS_{fit}$, where RSS_{fit} is the minimized value and ΔRSS is the deviation from RSS_{fit} when a parameter is raised or lowered from its optimal value indicated by the vertical dotted line. Symbols are individually calculated points spanning 4 orders of magnitude and solid lines are a third order spline interpolation.

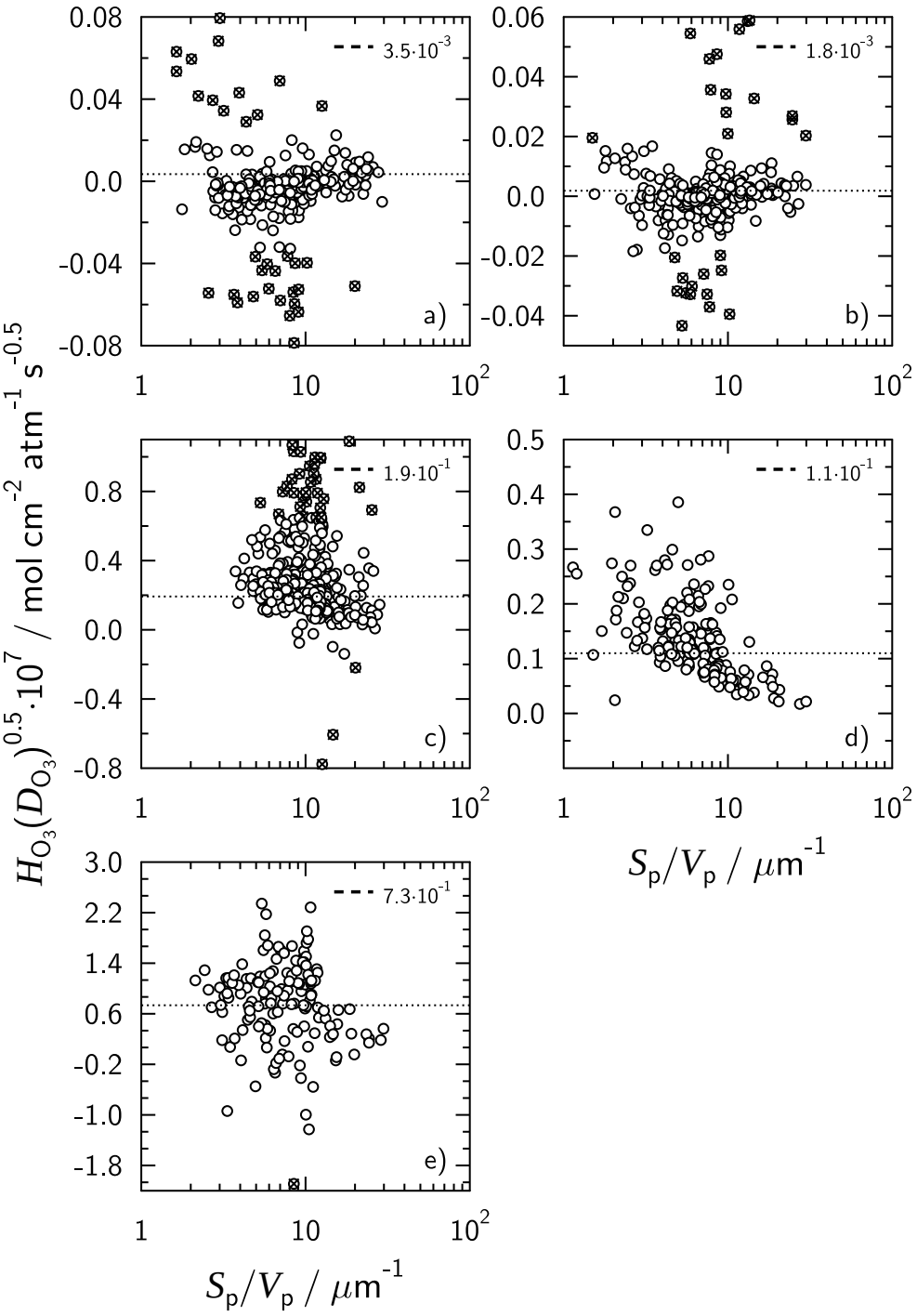

Figure S9: The product of Henry's Law coefficient for ozone, H_{O_3}, and the square root of the diffusion coefficient of ozone, D_{O_3}, or $H_{O_3}\sqrt{D_{O_3}}$, as a function of particle surface to volume ratio, S_p/V_p, at a relative humidity RH of a) 0%, b) 22%, c) 43%, d) 60% and e) 80%. Each data point is an individual particle. Values which deviate more than 3x the average deviation of the median are indicated with an "x". The dotted line is derived from fitted parameters and its value indicated in each panel.

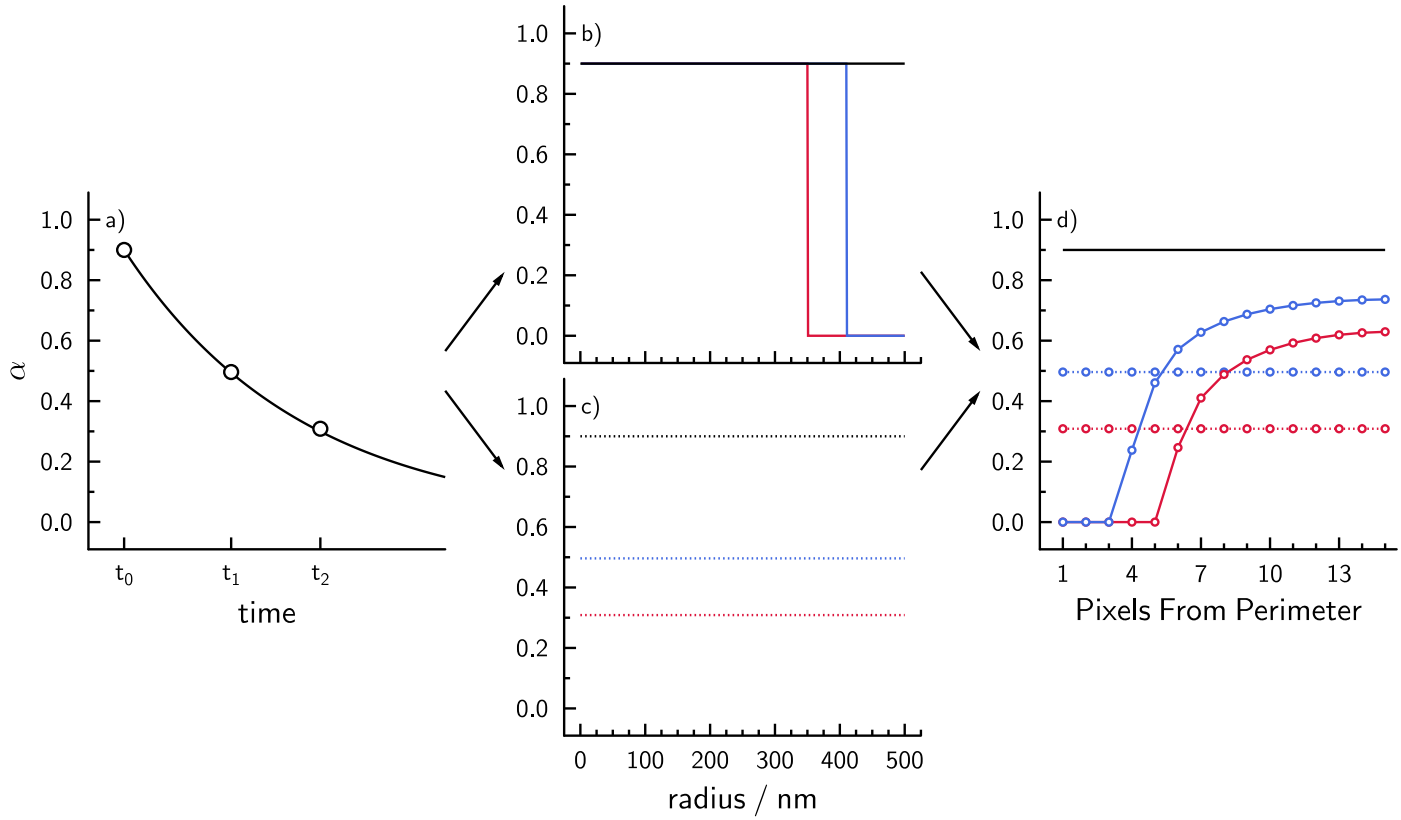

Figure S10: Examples of uniform and inhomogeneous 3-D radial and 2-D column integrated profiles of Fe^{2+} fraction, α. A hypothetical decay of α over time is shown in a) where t_0 is the initial value and t_1 and t_2 are at later arbitrary times. The symbols and line represent possible measurements and model predictions of α averaged over all particles. Radial particle profiles of α in 3-D are shown which are b) completely inhomogeneous and c) uniform, where black, blue and red color correspond to t_0, t_1 and t_2. When averaged over the entire particle, α in both b) and c) are equivalent and shown in a). Column integrated profiles are shown in d) where solid and dotted lines are from calculated from b) and c) respectively.

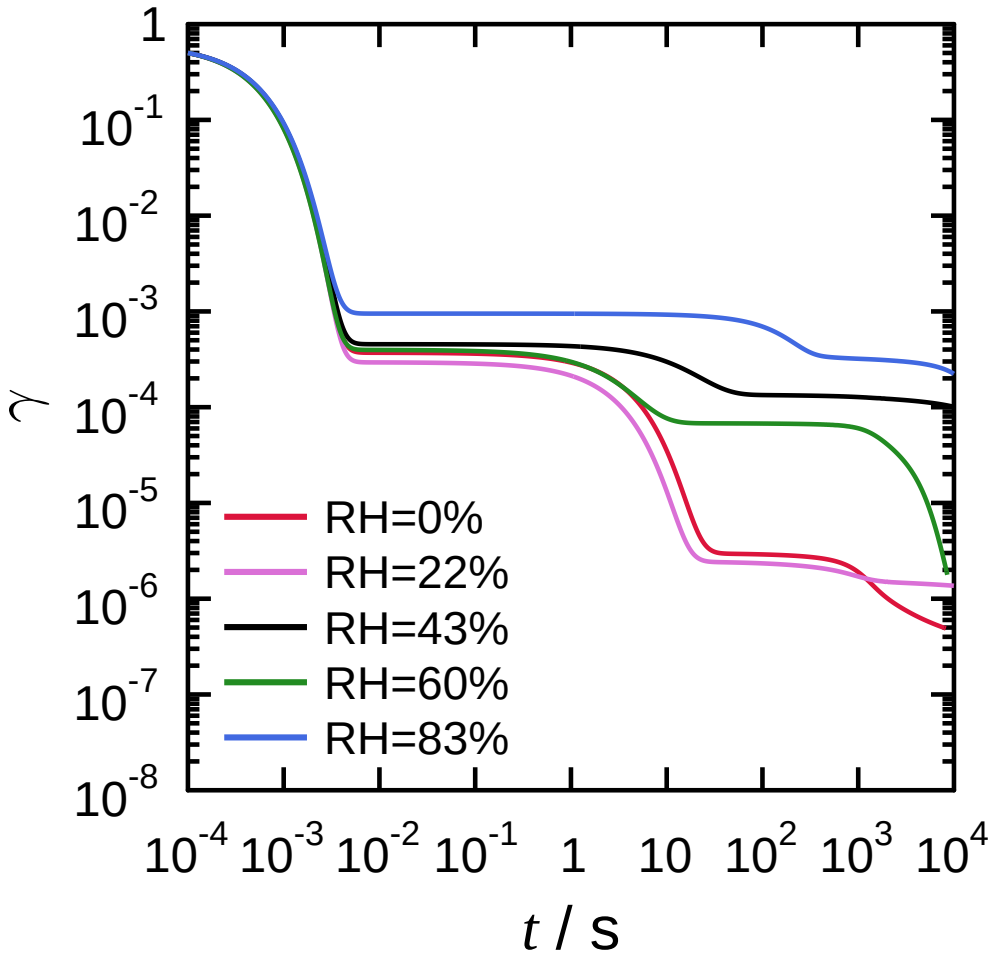

Figure S11: Calculated reactive uptake coefficients, γ, from the KM-SUB model as a function of time, t, for all experiments. Relative humidity, RH, is indicated.

References

[1] Q. Zhang, J. L. Jimenez, M. R. Canagaratna, J. D. Allan, H. Coe, I. Ulbrich, M. R. Alfarra, A. Takami, A. M. Middlebrook, Y. L. Sun, K. Dzepina, E. Dunlea, K. Docherty, P. F. DeCarlo, D. Salcedo, T. Onasch, J. T. Jayne, T. Miyoshi, A. Shimono, S. Hatakeyama, N. Takegawa, Y. Kondo, J. Schneider, F. Drewnick, S. Borrmann, S. Weimer, K. Demerjian, P. Williams, K. Bower, R. Bahreini, L. Cottrell, R. J. Griffin, J. Rautiainen, J. Y. Sun, Y. M. Zhang and D. R. Worsnop, *Geophys. Res. Lett.*, 2007, **34**, L13801.

[2] L. M. Russell, L. N. Hawkins, A. A. Frossard, P. K. Quinn and T. S. Bates, *Procc. Natl. Acad. Sci.*, 2010, **107**, 6652–6657.

[3] A. Laskin, M. K. Gilles, D. A. Knopf, B. Wang and S. China, *Annu. Rev. Anal. Chem.*, 2016, **9**, 117–143.

[4] J. Haywood and O. Boucher, *Rev. Geophys.*, 2000, **38**, 513–543.

[5] O. Boucher, D. Randall, P. Artaxo, C. Bretherton, G. Feingold, P. Forster, V.-M. Kerminen, Y. Kondo, H. Liao, U. Lohmann, P. Rasch, S. K. Satheesh, S. Sherwood, S. B. and Z. X.-Y., in *Climate Change 2013: The Physical Science Basis. Contribution of Working Group I to the Fifth Assessment Report of the Intergovernmental Panel on Climate Change*, ed. S. Fuzzi, J. Penner, V. Ramaswamy and C. Stubenrauch, Cambridge University Press, Cambridge, United Kingdom and New York, NY, USA, 2013, ch. 8. Clouds and Aerosols, pp. 571–657.

[6] T. Storelvmo, *Ann. Rev. Earth Pl. Sc.*, 2017, **45**, 199–222.

[7] D. A. Knopf, P. A. Alpert and B. Wang, *ACS Earth Space Chem.*, 2018, **2**, 168–202.

[8] Z. A. Kanji, L. A. Ladino, H. Wex, Y. Boose, M. Burkert-Kohn, D. J. Cziczo and M. Krämer, *Meteor. Mon.*, 2017, **58**, 1.1–1.33.

[9] J. H. Seinfeld and S. N. Pandis, *Atmospheric Chemistry and Physics - From Air Pollution to Climate Change*, John Wiley & Sons., Hoboken, NJ, 2nd edn, 2006.

[10] A. Tilgner, P. Bräuer, R. Wolke and H. Herrmann, *J. Atmos. Chem.*, 2013, **70**, 221–256.

[11] D. K. Farmer, C. D. Cappa and S. M. Kreidenweis, *Chem. Rev.*, 2015, **115**, 4199–4217.

[12] A. Laskin, R. C. Moffet, M. K. Gilles, J. D. Fast, R. A. Zaveri, B. Wang, P. Nigge and J. Shutthanandan, *J. Geophys. Res.*, 2012, **117**, D15302.

[13] M. Shiraiwa, Y. Li, A. P. Tsimpidi, V. A. Karydis, T. Berkemeier, S. N. Pandis, J. Lelieveld, T. Koop and U. Pöschl, *Nat. Comm.*, 2017, **8**, 15002.

[14] J. P. Reid, A. K. Bertram, D. O. Topping, A. Laskin, S. T. Martin, M. D. Petters, F. D. Pope and G. Rovelli, *Nat. Comm.*, 2018, **9**, 15002.

[15] B. R. Bzdek and J. P. Reid, *J. Chem. Phys.*, 2017, **147**, 220901.

[16] V. Perraud, E. A. Bruns, M. J. Ezell, S. N. Johnson, Y. Yu, M. L. Alexander, A. Zelenyuk, D. Imre, W. L. Chang, D. Dabdub, J. F. Pankow and B. J. Finlayson-Pitts, *Proc. Natl. Acad. Sci. U. S. A.*, 2012, **109**, 2836–2841.

[17] M. Shiraiwa, L. D. Yee, K. A. Schilling, C. L. Loza, J. S. Craven, A. Zuend, P. J. Ziemann and J. H. Seinfeld, *Proc. Natl. Acad. Sci. U. S. A.*, 2013, **110**, 11746–11750.

[18] L. Renbaum-Wolff, J. W. Grayson, A. P. Bateman, M. Kuwata, M. Sellier, B. J. Murray, J. E. Shilling, S. T. Martin and A. K. Bertram, *Proc. Natl. Acad. Sci. U. S. A.*, 2013, **110**, 8014–8019.

[19] J. H. Slade and D. A. Knopf, *Geophys. Res. Lett.*, 2014, **41**, 5297–5306.

[20] M. Shrivastava, S. Lou, A. Zelenyuk, R. C. Easter, R. A. Corley, B. D. Thrall, P. J. Rasch, J. D. Fast, S. L. Massey Simonich, H. Shen and S. Tao, *Proc. Natl. Acad. Sci. U. S. A.*, 2017, **114**, 1246–1251.

[21] J. Socorro, P. S. J. Lakey, L. Han, T. Berkemeier, G. Lammel, C. Zetzsch, U. Pöschl and M. Shiraiwa, *Environ. Sci. Technol.*, 2017, **51**, 13749–13754.

[22] M. Kanakidou, S. Myriokefalitakis and K. Tsigaridis, *Environ. Res. Lett.*, 2018, **13**, 063004.

[23] J. D. Smith, J. H. Kroll, C. D. Cappa, D. L. Che, C. L. Liu, M. Ahmed, S. R. Leone, D. R. Worsnop and K. R. Wilson, *Atmos. Chem. Phys.*, 2009, **9**, 3209–3222.

[24] M. N. Chan, H. Zhang, A. H. Goldstein and K. R. Wilson, *J. Phys. Chem. C*, 2014, **118**, 28978–28992.

[25] A. M. Arangio, J. H. Slade, T. Berkemeier, U. Pöschl, D. A. Knopf and M. Shiraiwa, *J. Phys. Chem. A*, 2015, **119**, 4533–4544.

[26] J. F. Davies and K. R. Wilson, *Chem. Sci.*, 2015, **6**, 7020–7027.

[27] H. Fan, M. R. Tinsley and F. Goulay, *J. Phys. Chem. A*, 2015, **119**, 11182–11190.

[28] M. M. Chim, C. T. Cheng, J. F. Davies, T. Berkemeier, M. Shiraiwa, A. Zuend and M. N. Chan, *Atmos. Chem. Phys.*, 2017, **17**, 14415–14431.

[29] M. M. Chim, C. Y. Chow, J. F. Davies and M. N. Chan, *J. Phys. Chem. A*, 2017, **121**, 1666–1674.

[30] M. J. Liu, A. A. Wiegel, K. R. Wilson and F. A. Houle, *J. Phys. Chem. A*, 2017, **121**, 5856–5870.

[31] K. C. Kwong, M. M. Chim, E. H. Hoffmann, A. Tilgner, H. Herrmann, J. F. Davies, K. R. Wilson and M. N. Chan, *ACS Earth Space Chem.*, 2018, **2**, 895–903.

[32] M. M. Chim, C. Y. Lim, J. H. Kroll and M. N. Chan, *ACS Earth Space Chem.*, 2018, **2**, 1323–1329.

[33] Z. Li, K. A. Smith and C. D. Cappa, *Atmos. Chem. Phys.*, 2018, **18**, 14585–14608.

[34] M. Shiraiwa, M. Ammann, T. Koop and U. Pöschl, *Proc. Natl. Acad. Sci. U. S. A.*, 2011, **108**, 11003–11008.

[35] S. Zhou, M. Shiraiwa, R. D. McWhinney, U. Pöschl and J. P. D. Abbatt, *Faraday Discuss.*, 2013, **165**, 391–406.

[36] S. S. Steimer, M. Lampimäki, E. Coz, G. Grzinic and M. Ammann, *Atmos. Chem. Phys.*, 2014, **14**, 10761–10772.

[37] S. S. Steimer, T. Berkemeier, A. Gilgen, U. K. Krieger, T. Peter, M. Shiraiwa and M. Ammann, *Phys. Chem. Chem. Phys.*, 2015, **17**, 31101–31109.

[38] M. I. Jacobs, B. Xu, O. Kostko, N. Heine, M. Ahmed and K. R. Wilson, *J. Phys. Chem. A*, 2016, **120**, 8645–8656.

[39] N. Heine, F. A. Houle and K. R. Wilson, *Environ. Sci. Technol.*, 2017, **51**, 13740–13748.

[40] U. Pöschl, Y. Rudich and M. Ammann, *Atmos. Chem. Phys.*, 2007, **7**, 5989–6023.

[41] M. Ammann and U. Pöschl, *Atmos. Chem. Phys.*, 2007, **7**, 6025–6045.

[42] C. Pfrang, M. Shiraiwa and U. Pöschl, *Atmos. Chem. Phys.*, 2010, **10**, 4537–4557.

[43] M. Shiraiwa, C. Pfrang and U. Pöschl, *Atmos. Chem. Phys.*, 2010, **10**, 3673–3691.

[44] M. Shiraiwa, C. Pfrang, T. Koop and U. Pöschl, *Atmos. Chem. Phys.*, 2012, **12**, 2777–2794.

[45] T. Berkemeier, A. J. Huisman, M. Ammann, M. Shiraiwa, T. Koop and U. Pöschl, *Atmos. Chem. Phys.*, 2013, **13**, 6663–6686.

[46] F. A. Houle, W. D. Hinsberg and K. R. Wilson, *Phys. Chem. Chem. Phys.*, 2015, **17**, 4412–4423.

[47] T. Berkemeier, S. S. Steimer, U. K. Krieger, T. Peter, U. Pöschl, M. Ammann and M. Shiraiwa, *Phys. Chem. Chem. Phys.*, 2016, **18**, 12662–12674.

[48] A. A. Wiegel, M. J. Liu, W. D. Hinsberg, K. R. Wilson and F. A. Houle, *Phys. Chem. Chem. Phys.*, 2017, **19**, 6814–6830.

[49] F. A. Houle, A. A. Wiegel and K. R. Wilson, *Environ. Sci. Technol.*, 2018, **52**, 13774–13781.

[50] F. A. Houle, A. A. Wiegel and K. R. Wilson, *J. Phys. Chem. Lett.*, 2018, **9**, 1053–1057.

[51] L. Lee and K. Wilson, *J. Phys. Chem. A*, 2016, **120**, 6800–6812.

[52] T. J. Conocchioli, E. J. Hamilton and N. Sutin, *J. Am. Chem. Soc.*, 1965, **87**, 926–927.

[53] J. Hoigné, H. Bader, W. Haag and J. Staehelin, *Water Res.*, 1985, **19**, 993–1004.

[54] T. Løegager, J. Holcman, K. Sehested and T. Pedersen, *Inorganic Chemistry*, 1992, **31**, 3523–3529.

[55] O. Pestovsky and A. Bakac, *Inorg. Chem.*, 2006, **45**, 814–820.

[56] S. Enami, Y. Sakamoto and A. J. Colussi, *Proc. Natl. Acad. Sci. U. S. A.*, 2014, **111**, 623–628.

[57] R. C. Moffet, H. Furutani, T. C. Rödel, T. R. Henn, P. O. Sprau, A. Laskin, M. Uematsu and M. K. Gilles, *J. Geophys. Res.*, 2012, **117**, D07204.

[58] T. D. Jickells, Z. S. An, K. K. Andersen, A. R. Baker, G. Bergametti, N. Brooks, J. J. Cao, P. W. Boyd, R. A. Duce, K. A. Hunter, H. Kawahata, N. Kubilay, J. laRoche, P. S. Liss, N. Mahowald, J. M. Prospero, A. J. Ridgwell, I. Tegen and R. Torres, *Science*, 2005, **308**, 67–71.

[59] M. T. Maldonado and N. M. Price, *Deep-Sea Res. Pt. II*, 1999, **46**, 2447–2473.

[60] A. Baker and P. Croot, *Mar. Chem.*, 2010, **120**, 4–13.

[61] Z. Shi, M. D. Krom, T. D. Jickells, S. Bonneville, K. S. Carslaw, N. Mihalopoulos, A. R. Baker and L. G. Benning, *Aeolian Res.*, 2012, **5**, 21–42.

[62] H. Chen and V. H. Grassian, *Environ. Sci. Technol.*, 2013, **47**, 10312–10321.

[63] R. Paris and K. V. Desboeufs, *Atmos. Chem. Phys.*, 2013, **13**, 4895–4905.

[64] A. Ito and Z. Shi, *Atmos. Chem. Phys.*, 2016, **16**, 85–99.

[65] N. M. Mahowald, R. Scanza, J. Brahney, C. L. Goodale, P. G. Hess, J. K. Moore and J. Neff, *Curr. Clim. Change Rep.*, 2017, **3**, 16–31.

[66] K. W. Dawson, M. D. Petters, N. Meskhidze, S. S. Petters and S. M. Kreidenweis, *J. Geophys. Res.*, 2016, **121**, 11803–11818.

[67] I. A. Challen, in *Food Hydrocolloids: Structures, Properties, and Functions*, ed. K. Nishinari and E. Doi, Plenum Press, New York, NY, USA, 1993, ch. Xanthan Gum: A Multifunctional Stabiliser for Food Products, pp. 135–140.

[68] B. Katzbauer, *Polym. Degrad. Stabil.*, 1998, **59**, 81–84.

[69] S. Basu, U. S. Shivhare and A. S. Mujumdar, *Dry. Technol.*, 2007, **25**, 1581–1586.

[70] U. Passow and A. L. Alldredge, *Limnol. Oceanogr.*, 1995, **40**, 1326–1335.

[71] U. Passow, *Prog.Oceanogr.*, 2002, **55**, 287–333.

[72] A. Engel, in *Practical Guidelines for the Analysis of Seawater*, ed. O. Wurl, CRC Press, Boca Raton, FL, USA, 2009, ch. 7. Determination of Marine Gel Particles, pp. 125–142.

[73] J. Y. Aller, J. C. Radway, W. P. Kilthau, D. W. Bothe, T. W. Wilson, R. D. Vaillancourt, P. K. Quinn, D. J. Coffman, B. J. Murray and D. A. Knopf, *Atmos. Environ.*, 2017, **154**, 331–347.

[74] R. A. Speers and M. A. Tung, *J. Food Sci.*, 1986, **51**, 96–98.

[75] N. B. Wyatt and M. W. Liberatore, *J. Appl. Polym. Sci.*, 2009, **114**, 4076–4084.

[76] M. Shiraiwa, U. Pöschl and D. A. Knopf, *Environ. Sci. Technol.*, 2012, **46**, 6630–6636.

[77] S. Steigenberger, P. J. Statham, C. Völker and U. Passow, *Biogeosci.*, 2010, **7**, 109–119.

[78] R. D. Shannon, *Acta Cryst.*, 1976, **32**, 751–767.

[79] R. S. Smith and B. D. Kay, *Nature*, 1999, **398**, 788–791.

[80] D. Bergmann, G. Furth and C. Mayer, *Int. J. Biol. Macromol.*, 2008, **43**, 245–251.

[81] A. Einstein, *Ann. Phys.*, 1905, **17**, 549–560.

[82] W. Sutherland, *Philos. Mag.*, 1905, **9**, 781–785.

[83] D. M. Lienhard, A. J. Huisman, U. K. Krieger, Y. Rudich, C. Marcolli, B. P. Luo, D. L. Bones, J. P. Reid, A. T. Lambe, M. R. Canagaratna, P. Davidovits, T. B. Onasch, D. R. Worsnop, S. S. Steimer, T. Koop and T. Peter, *Atmos. Chem. Phys.*, 2015, **15**, 13599–13613.

[84] F. H. Marshall, R. E. H. Miles, Y.-C. Song, P. B. Ohm, R. M. Power, J. P. Reid and C. S. Dutcher, *Chem. Sci.*, 2016, **7**, 1298–1308.

[85] P. D. Oliveira, R. C. Michel, A. J. A. McBride, A. S. Moreira, R. F. T. Lomba and C. T. Vendruscolo, *PLOS ONE*, 2013, **8**, 1–7.

[86] M. Mobin and M. Rizvi, *Carbohyd. Polym.*, 2016, **136**, 384–393.

[87] A. K. Biń, *Ozone-Sci. Eng.*, 2006, **28**, 67–75.

[88] R. Battino, T. R. Rettich and T. Tominaga, *J. Phys. Chem. Ref. Data*, 1983, **12**, 163–178.

[89] P. Corral Arroyo, T. Bartels-Rausch, P. A. Alpert, S. Dumas, S. Perrier, C. George and M. Ammann, *Environ. Sci. Technol.*, 2018, **52**, 7680–7688.

[90] L.-K. Ju and C. S. Ho, *Can. J. Chem. Eng.*, 1989, **67**, 471–477.

[91] A. L. Rose and T. D. Waite, *Environ. Sci. Technol.*, 2002, **36**, 433–444.

[92] D. W. King, H. A. Lounsbury and F. J. Millero, *Environ. Sci. Technol.*, 1995, **29**, 818–824.

[93] R. Sander, *Atmos. Chem. Phys.*, 2015, **15**, 4399–4981.

[94] Y. P. Lee, M. Fujii, K. Terao, T. Kikuchi and C. Yoshimura, *Water Res.*, 2016, **103**, 160–169.

[95] D. R. Worsnop, J. W. Morris, Q. Shi, P. Davidovits and C. E. Kolb, *Geophys. Res. Lett.*, 2002, **29**, GL015542.

[96] D. R. Hanson and E. R. Lovejoy, *Science*, 1995, **267**, 1326–1328.

[97] P. J. Flory and T. G. Fox, *J. Am. Chem. Soc.*, 1951, **73**, 1904–1908.

[98] J. H. Kroll and J. H. Seinfeld, *Atmos. Environ.*, 2008, **42**, 3593–3624.

[99] M. Hallquist, J. C. Wenger, U. Baltensperger, Y. Rudich, D. Simpson, M. Claeys, J. Dommen, N. M. Donahue, C. George, A. H. Goldstein, J. F. Hamilton, H. Herrmann, T. Hoffmann, Y. Iinuma, M. Jang, M. E. Jenkin, J. L. Jimenez, A. Kiendler-Scharr, W. Maenhaut, G. McFiggans, T. F. Mentel, A. Monod, A. S. H. Prévôt, J. H. Seinfeld, J. D. Surratt, R. Szmigielski and J. Wildt, *Atmos. Chem. Phys.*, 2009, **9**, 5155–5236.

[100] H. Herrmann, T. Schaefer, A. Tilgner, S. A. Styler, C. Weller, M. Teich and T. Otto, *Chem. Rev.*, 2015, **115**, 4259–4334.

[101] R. Volkamer, F. San Martini, L. T. Molina, D. Salcedo, J. L. Jimenez and M. J. Molina, *Geophys.Res. Lett.*, 2007, **34**, L19807.

[102] T. P. Riedel, Y.-H. Lin, Z. Zhang, K. Chu, J. A. Thornton, W. Vizuete, A. Gold and J. D. Surratt, *Atmos. Chem. Phys.*, 2016, **16**, 1245–1254.

[103] X. Zhang, A. T. Lambe, M. A. Upshur, W. A. Brooks, A. Gray Bé, R. J. Thomson, F. M. Geiger, J. D. Surratt, Z. Zhang, A. Gold, S. Graf, M. J. Cubison, M. Groessl, J. T. Jayne, D. R. Worsnop and M. R. Canagaratna, *Environ. Sci. Technol.*, 2017, **51**, 5932–5940.

[104] V. F. McNeill, J. L. Woo, D. D. Kim, A. N. Schwier, N. J. Wannell, A. J. Sumner and J. M. Barakat, *Environ. Sci. Technol.*, 2012, **46**, 8075–8081.

765 [105] Y. Zhang, Y. Chen, A. T. Lambe, N. E. Olson, Z. Lei, R. L. Craig, Z. Zhang, A. Gold, T. B. Onasch, J. T. Jayne,
766 D. R. Worsnop, C. J. Gaston, J. A. Thornton, W. Vizuete, A. P. Ault and J. D. Surratt, *Environ. Sci. Technol.*
767 *Lett.*, 2018, **5**, 167–174.

768 [106] T. Huthwelker, V. Zelenay, M. Birrer, A. Krepelova, J. Raabe, G. Tzvetkov, M. G. C. Vernooij and M. Ammann,
769 *Rev. Sci. Instrum.*, 2010, **81**, 113706.

770 [107] J.-D. Förster, C. Pöhlker, C. Gurk, M. Lamneck, M. Ammann, U. Pöschl and M. O. Andreae, *Atmos. Mech. Tech.*,
771 2019, **XX**, to be submitted.

772 [108] D. M. Murphy and T. Koop, *Q. J. R. Meteorol. Soc.*, 2005, **131**, 1539–1565.

773 [109] J. Raabe, G. Tzvetkov, U. Flechsig, M. Böge, A. Jaggi, B. Sarafimov, M. G. C. Vernooij, T. Huthwelker, H. Ade,
774 D. Kilcoyne, T. Tyliszczak, R. H. Fink and C. . Quitmann, *Rev. Sci. Instrum.*, 2008, **79**, 113704.

775 [110] R. C. Moffet, T. Henn, A. Laskin and M. K. Gilles, *Anal. Chem.*, 2010, **82**, 7906–7914.

776 [111] G. Cressey, C. M. B. Henderson and G. van der Laan, *Phys. Chem. of Miner.*, 1993, **20**, 111–119.

777 [112] L. A. J. Garvie, A. J. Craven and R. Brydson, *Am. Mineral.*, 1994, **79**, 411–425.

778 [113] P. Vanýsek, in *CRC Handbook of Chemistry and Physics, 82*$^{\text{nd}}$ *edition*, ed. D. R. Lide, CRC Press, Boca Raton, Fl,
779 USA, 2001, ch. Ionic conductivity and diffusion at infinite dilution, pp. 5–95.